

LITHOSPHERIC STRUCTURE OF THE CENTRAL ANDEAN FORE-ARC FROM
GRAVITY DATA MODELING: IMPLICATION FOR PLATE COUPLING

by

GREG GUSHURST

REZENE MAHATSENTE, COMMITTEE CHAIR
IBRAHIM ÇEMEN
BO ZHANG
TONY SMITHSON

A THESIS

Submitted in partial fulfillment of the requirements
for the degree of Master of Science
in the Department of Geological Sciences
in the Graduate School of
The University of Alabama

TUSCALOOSA, ALABAMA

2019

Copyright Greg Gushurst 2019
ALL RIGHTS RESERVED

ABSTRACT

Geodetic and seismological data indicates that the Central Andes subduction zone is highly coupled. To understand the plate locking mechanism within the Central Andes, I developed 2.5-D gravity models of the lithosphere and assessed the region's isostatic state. The densities within the gravity models are based on satellite and surface gravity data and constrained by previous tomographic studies. The gravity models indicate a high density ($\sim 2940 \text{ kg m}^{-3}$) fore-arc structure in the overriding South American continental lithosphere, which is higher than the average density of continental crust. This structure produces an anomalous pressure (20 - 40 MP) on the subducting Nazca plate, contributing to intraplate coupling within the Central Andes. The anomalous lithostatic pressure and buoyancy force may be controlling plate coupling and asperity generation in the Central Andes. The high density fore-arc structure could be a batholith or ophiolite emplaced onto continental crust.

The isostatic state of the Central Andes and Nazca plate is assessed based on residual topography (difference between observed and isostatic topography). The West-Central Andes and Nazca ridge have $\sim 0.78 \text{ km}$ of residual topography, indicating under compensation. The crustal thickness beneath the West-Central Andes may not be sufficient to isostatically support the observed topography. This residual topography may be partially supported by small scale convective cells in the mantle wedge.

The residual topography in the Nazca ridge may be attributed to density differences between the subducting Nazca slab and Nazca ridge. The high density of the subducted Nazca

slab has a downward buoyancy force, while the less dense Nazca ridge provides an upward buoyancy force. These two forces may effectively raise the Nazca ridge to its current day elevation.

DEDICATION

This thesis is dedicated to everyone who helped me through my Masters degree. I would like to personally thank my friends, family, and colleagues for their dedicated support.

LIST OF ABBREVIATIONS AND SYMBOLS

2.5-D	Two and a half dimension
3-D	Three dimension
Ca.	Circa
<i>Cm</i>	Centimeter
EIGEN	European Improved Gravity Model of the Earth
<i>Km</i>	Kilometer
<i>mGal</i>	Milligal
<i>MPa</i>	Mega-Pascal
M_w	Magnitude (Richter)
<i>yr</i>	Year

ACKNOWLEDGEMENTS

I would like to thank Dr. Rezene Mahatsente for taking me on as his student and providing guidance, support, and encouragement throughout my Master's degree. He made my time here at The University of Alabama an unforgettable memory and experience. In addition, I would also like to thank the Department of Geological Sciences and the Geological Sciences Advisory Board for their support throughout my tenure here at The University of Alabama.

Finally, I would like to express my gratitude to my family, friends, and loving girlfriend for their unending support and motivation. If not for them I would not have been able to succeed as I have, both as an academic and a person. This degree is as much mine as it is theirs.

Thank you to everyone who has helped me through this period of my career

CONTENTS

ABSTRACT.....	ii
DEDICATION.....	iv
LIST OF ABBREVIATIONS AND SYMBOLS.....	v
ACKNOWLEDGEMENTS.....	vi
LIST OF TABLES.....	ix
LIST OF FIGURES.....	x
1. INTRODUCTION.....	1
2. GEOLOGIC SETTING.....	5
3. GRAVITY DATABASE AND METHODOLOGY.....	9
3.1. Wavelength Filtering.....	10
3.2. Isostasy Modelling.....	11
4. INITIAL MODEL & CONSTRAINTS.....	12
5. RESULTS AND DISCUSSION.....	16
5.1. Gravity Anomaly Analysis.....	16
5.2. Lithospheric Structure & Locking Mechanism.....	21
5.3. Isostatic State of central Andes.....	33

6. CONCLUSIONS.....	39
REFERENCES	41
APPENDIX.....	48
Codes written for gravity corrections and analysis. :.....	48
Dynamic Topography:.....	50

LIST OF TABLES

Table 1. Densities and P-wave velocities used in 2.5-D gravity modeling.....	13
Table 2. Final densities used in 2.5-D gravity models and their uncertainty.....	14

LIST OF FIGURES

- Figure 1.** Topographic map for the Peru-Chile subduction zone showing earthquakes, volcanoes, and trench. Black lines with squares indicate locations of gravity models. The elevation data are from the National Oceanic and Atmospheric Administration. The earthquake epicenters (events from 1960 - 2019) are from the USGS Earthquake Archive..... 4
- Figure 2.** A geologic map of the Peru-Chile subduction zone highlighting the various geologic structures. Abbreviations: CC Coastal Cordillera, CD Coastal Depression, FP Fore-arc Precordillera, WC Western Cordillera, AT Altiplano, EC Eastern Cordillera (after Charrier et al., 2013). 8
- Figure 3.** A complete Bouguer Anomaly map of the Peru-Chile subduction zone. The saw tooth line is the location of the trench and the straight line is the Nazca Ridge..... 18
- Figure 4.** (A) Regional Bouguer anomaly shows the large-scale structures. The crustal root is seen as the long negative anomaly trending NW-SE. (B) Residual Bouguer anomaly shows shallow structures. These anomalies can be attributed to volcanic centers and cordilleras. 20
- Figure 5.** 2.5-D gravity model of the central Andes subduction at (A) 20° S and (B) 19°. The two models located within the southern seismic gap zone. Numbers indicate densities of structures in kg m^{-3} . White dots are earthquake hypocenters from the USGS database from 1960 - 2019. 23
- Figure 6.** Vertical stress anomaly calculated on top of the subducting Nazca plate. (A) at 20°S (B) at 19°S. 24
- Figure 7.** 2.5-D gravity model of the central Andes subduction at 16°S, a loosely coupled region. Numbers indicate densities of structures in kg m^{-3} . White dots are earthquake hypocenters from the USGS database (events from 1960 – 2019). 25
- Figure 8.** Vertical stress anomaly calculated on top of the subducting Nazca plate 16°S. 26
- Figure 9.** GPS derived coupling coefficients for the (Left) Peru (Right) Chile subduction zone. (Chlieh et al., 2011). The black and green arrows are observed and predicted interseismic GPS displacements, respectively. 27

Figure 10. 2.5-D gravity model of the central Andes subduction at 12°S, a loosely coupled region. Numbers indicate densities of structures in kg m⁻³. White dots are earthquake hypocenters from the USGS database (events from 1960 – 2019)..... 28

Figure 11. 2.5-D gravity model of the central Andes subduction at 69°W. Numbers indicate densities of structures in kg m⁻³. White dots are earthquake hypocenters from the USGS database (events from 1960 – 2019). 29

Figure 12. 2.5-D gravity model of the central Andes subduction at 75.5°W. Numbers indicate densities of structures in kg m⁻³. White dots are earthquake hypocenters from the USGS database (events from 1960 – 2019)..... 30

Figure 13. A map view of the subducting Nazca Slab. The red circle indicates approximate area of coupling due to the high-density structure. The yellow circle indicates approximate area of coupling due to the low-density Nazca ridge. The black arrow is the projection of the incoming Nazca ridge. 31

Figure 14. A South-East to North-West view of the subducting Nazca slab. The red circle indicates approximate area of coupling due to the high-density structure. The yellow circle indicates approximate area of coupling due to the low-density Nazca ridge. The black arrow is the projection of the incoming Nazca ridge. 32

Figure 15. Isostatic topography of the Central Andes based on the Vennig-Meinesz, 1939, model. The saw tooth line indicates position of the trench..... 35

Figure 16. Residual topography of the Central Andes. The saw tooth line indicates location of the trench and the straight line is the Nazca Ridge..... 37

1. INTRODUCTION

Large earthquakes commonly occur in Pacific subduction zones where the greatest tectonic strain accumulates (Moreno et al., 2011). The Cascadia subduction zone, in the northwest of North America, has produced earthquakes greater than M_w 8 every 500 years (Satake et al., 1996). The Kamchatka subduction zone in the Pacific Northwest had a M_w 9 earthquake in 1952 (Burgmann, 2005) and, south-west of this zone, 10 major earthquakes of $M_w \geq 7.5$ have occurred in the Japan-Kuril trench in the last century (Utsu, 1999). The area of this study, the Peru-Chile subduction zone (Figure 1), frequently experiences major earthquakes that are among some of the largest recorded ($M_w > 8.5$; Lomnitz, 2004; Cisternas et al., 2005; Allmendinger and Gonzalez, 2010; Tassara, 2010). The largest earthquake ever recorded by instruments, M_w 9.5, occurred near Valdivia, Chile, in 1960 (Moreno et al., 2011). In addition to the Valdivia earthquake, the South American subduction zone has had numerous large earthquakes in the past few centuries resulting in multiple full-length ruptures of the entire margin (Lomnitz, 2004). The subduction zone is well studied in the regions of high seismic moment release (asperity). Areas of low asperity, seismic gaps, are seen throughout the subduction zone (Bilek, 2010). Two noteworthy gaps are present at the Peru-Chile border (18°S , 71°W) to (21°S , 71°W) and northern Peru (1°S , 81°W) to (11°S , 79°W). These seismic gaps have experienced large earthquakes with magnitudes $M_w > 8.5$ in 1746, 1868, and 1877 (Dorbath et al., 1990). The 1877 Iquique megathrust, M_w 8.5 – 9.0, ruptured Ca. 450 km of the thrust fault (Comte and Pardo, 1991). Several earthquakes with magnitude $M_w < 8.5$ have occurred in the

Central Andes, notably the 2014 Iquique earthquake with $M_w = 8.2$, the 2001 Arequipa earthquake with $M_w = 8.4$, and the 2007 Pisco earthquake with $M_w = 8.0$. The 2014 Iquique earthquake, M_w 8.2, experienced a rupture of Ca. 150 km, far less than the 1877 megathrust, Ca. 450 km (Lay et al., 2014; Yagi et al., 2014; Meng et al., 2015). Even with the energy released from these recent earthquakes, it is expected that the zone still possesses enough elastic energy to experience similar events to the previous megaquakes (Chlieh et al., 2011). Earthquakes in this subduction zone are primarily caused by the Nazca plate subducting under the South American Plate (Figure 1).

Geodetic measurements in the area indicate regions of high plate coupling, centered around the Central Andes seismic gap zone up to a depth of 50 km, assuming elastic behavior (Chlieh et al., 2011). The correlation between highly coupled zones and megathrust earthquakes has been shown by previous studies (Moreno et al., 2010; Ruiz et al., 2014; Schurr et al., 2014). Additionally, previous studies have shown mass redistribution or fluid pressure variations, seen in vertical gravity gradient changes over time, to potentially indicate areas of asperity generation (Álvarez et al., 2015)

What is not clearly understood is the mechanism that controls asperity generation and hence the seismic gaps. As shown by Gutscher et al., in 2000, geometry of the subducting Nazca plate plays a role in plate coupling. A shallow subduction leads to an increase of contact area resulting in greater compressional strain (Lallemand et al., 2005). Previous research shows a shallow slab in the north that transitions to a steep slab in the south (Gutscher et al., 2000; Lallemand et al., 2005; Tassara, 2005; Moreno et al., 2009).

Two hypotheses have been suggested to explain the locking mechanism of the Peru-Chile subduction zone: The first hypothesis states that a high-density structure, within the fore-arc,

produces a downward buoyancy force, locking the overriding and subducting plates (Tassara, 2010; Schaller et al., 2015). The second hypothesis is that low density oceanic features on the subducting slab pull the slab upwards during the subduction process and thereby lock the plate interfaces (Bilek, 2010; Wang and Bilek, 2011; Alvarez et al., 2014). In this study I examine the locking mechanism of the plate interface in the Central Andes based on gravity data modelling.

Six 2.5-D gravity models, representative of the Central Andes subduction zone, are presented. The models show the crust and upper mantle structure within the region and help assess the plate locking mechanism in the Central Andes. The density models are based on terrestrial and satellite gravity data and constrained by velocity models from seismic tomography and receiver function.

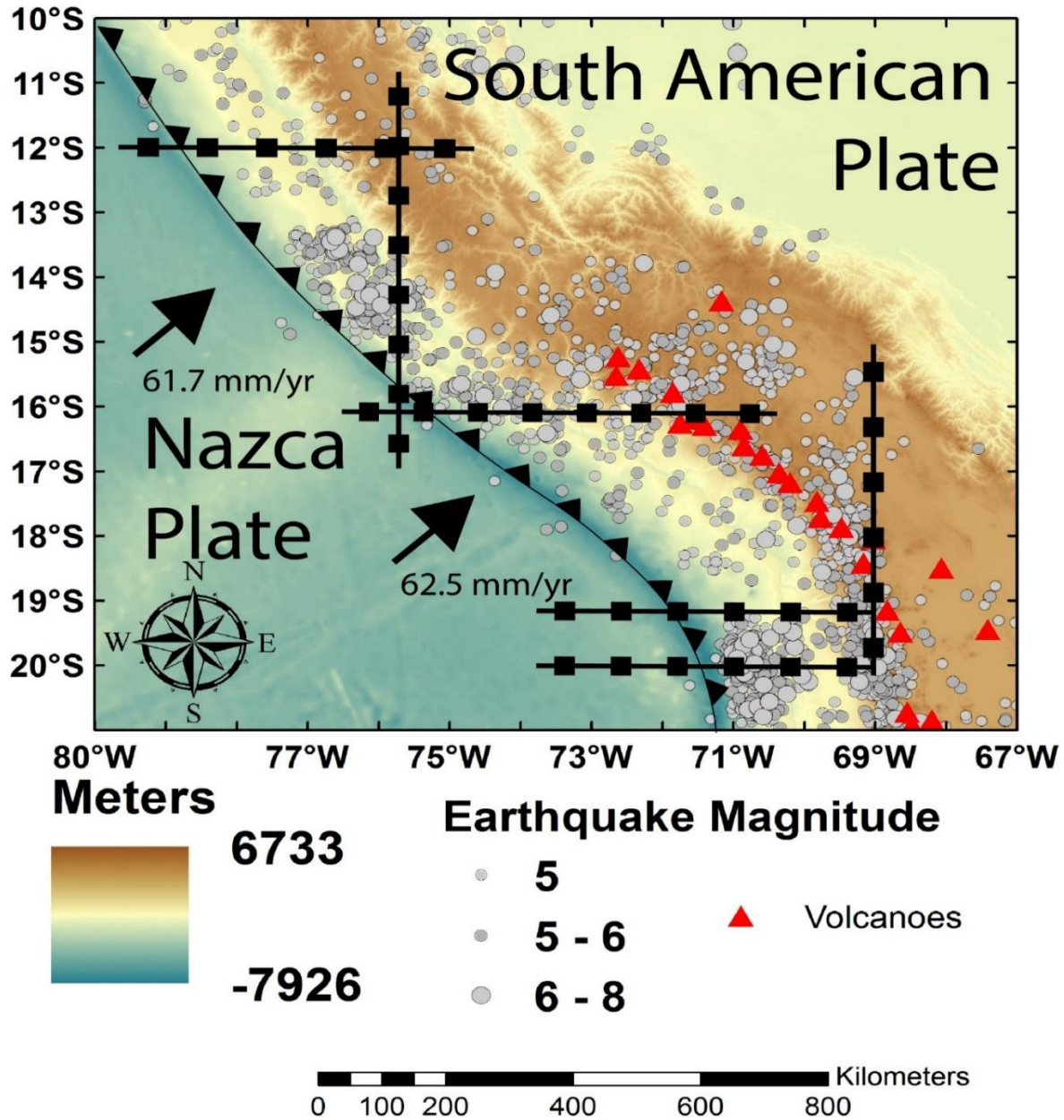


Figure 1. Topographic map for the Peru-Chile subduction zone showing earthquakes, volcanoes, and trench. Black lines with squares indicate locations of gravity models. The elevation data are from the National Oceanic and Atmospheric Administration. The earthquake epicenters (events from 1960 - 2019) are from the USGS Earthquake Archiv

2. GEOLOGIC SETTING

The Andes Mountains are a result of the convergence between the Farallon and the South American plates, following the breakup of the super-continent, Gondwana, in the Jurassic (Pardo-Casas and Molnar, 1987; Mpodozis and Ramos, 1989; Somoza, 1998; Somoza and Zaffarana, 2008). Due to the convergence of the two plates, four successive arcs, the coastal cordillera, pre-cordillera, western cordillera, and eastern cordillera, developed in the mountain range (Figure 2). Each of these arcs has a separation from the previous up to 100 km (Scheuber and Reutter, 1992; Schmitz, 1994; Allmendinger et al., 1997; Ramos, 2010; Folguera and Ramos, 2011; Scheuber et al., 2012). In the Late Oligocene the Farallon plate split into the Cocos plate, in the north, and the Nazca plate, in the south, due to a change in the convergence angle and an increase in the speed of the southern part of the Farallon plate (Tassara, 2010).

After the splitting of the Farallon plate into the Cocos and Nazca plates, the convergence rate of the Nazca plate with South America peaked in the Early-Mid Miocene, 15 cm/yr, (Tassara, 2005, 2010) and has been on the downward trend since, with the current rate at 6.5 cm/yr (Pardo-Casas and Molnar, 1987; Somoza, 1998).

It is estimated that nearly 200 km of the South American plate has been eroded around the Peru-Chile subduction zone (von Huene and Scholl, 1991). This erosion is suspected because, around the Antofagasta area, the ancient Jurassic volcanic arc is currently 75 km east of the trench and 35 km above the subducting Nazca Plate (Rutland, 1971; Allmendinger and González, 2010). In addition to the location of the Jurassic volcanic arc, previous studies have

shown that the area is lacking an accretionary prism and normal faults are observed from the Coastal Cordillera up to the trench (von Huene and Scholl, 1991; von Huene and Ranero, 2003).

The current formation of the Andes Mountains encompasses an area of 800,000 km² and has elevations above 6 km, in the central region, and an average of 3.8 km elsewhere (Tassara et al., 2006). The subduction zone is segmented into four different latitudinal pieces: northern (10°N–5°S), central (5°S–33.5°S), southern (33.5°–46.5°S) and austral (46.5°–56°S) Andes, each varying in age, topography, and volcanism (Tassara et al., 2006). The oceanic crust is the youngest in the central region, less than 1 Myr at 20°S, increasing in age to the north, 28 Myr at 5°S, and the south, 48 Myr at 46.5°S (Tassara et al., 2006; Tassara, 2010). The area of this study, the Central Andes, can be classified in a longitudinal sense as well (Figure 2). The western most structure is the trench that runs approximately 5900 km down the coast and on average 64 km off the coast of South America. The deepest part of the trench reaches down to 8 km (Álvarez et al., 2014). East of the trench is the Coastal Cordillera, an area of hills, less than 1.2 km in altitude, and valleys, composed of Mesozoic rock (Rutledge and Mahatsente, 2017). Eastward of the Coastal Cordillera is the Coastal Depression, an area composed of Lower Cretaceous volcanic sediments and plutons (Prezzi et al., 2009; Tassara, 2005). The Fore-arc Precordillera is east of the Coastal Depression and is composed of Paleozoic basement, Eocene magmatic rocks, and Mesozoic and Tertiary sedimentary and volcanic rocks (Tassara, 2005; Scheuber et al., 2012). The greatest elevation, 6 km, in the Andes is seen in the Western Cordillera, an area east of the fore-arc Precordillera (Tassara et al., 2006). Flanking the Western Cordillera is the Altiplano-Puna plateau, this plateau is comprised of Mesozoic-Cenozoic sedimentary infill that can be 10 km thick (Prezzi et al., 2009). The Eastern Cordillera is the easternmost part of the Andes and is

comprised of Precambrian to Paleozoic sedimentary rocks within a system of thrust belts (Prezzi et al., 2009; Rutledge and Mahatsente, 2017).

Within the region, the Nazca Ridge subducts beneath the South American plate. This oceanic feature is less dense and thicker than the surrounded oceanic crust and experiences an upwards buoyancy force (Gutscher et al., 2000; Hunen et al., 2002). This upwards buoyancy force is strong enough to decrease the subduction angle of the plate (Gutscher et al., 2000; Hunen et al., 2002). In addition to the buoyancy force, the motion of the overriding plate, South America, has the potential to cause regional changes in subduction angle (Gutscher et al., 2000, Husen et al., 2002). The variation in subduction angle can result in plate coupling within the region.

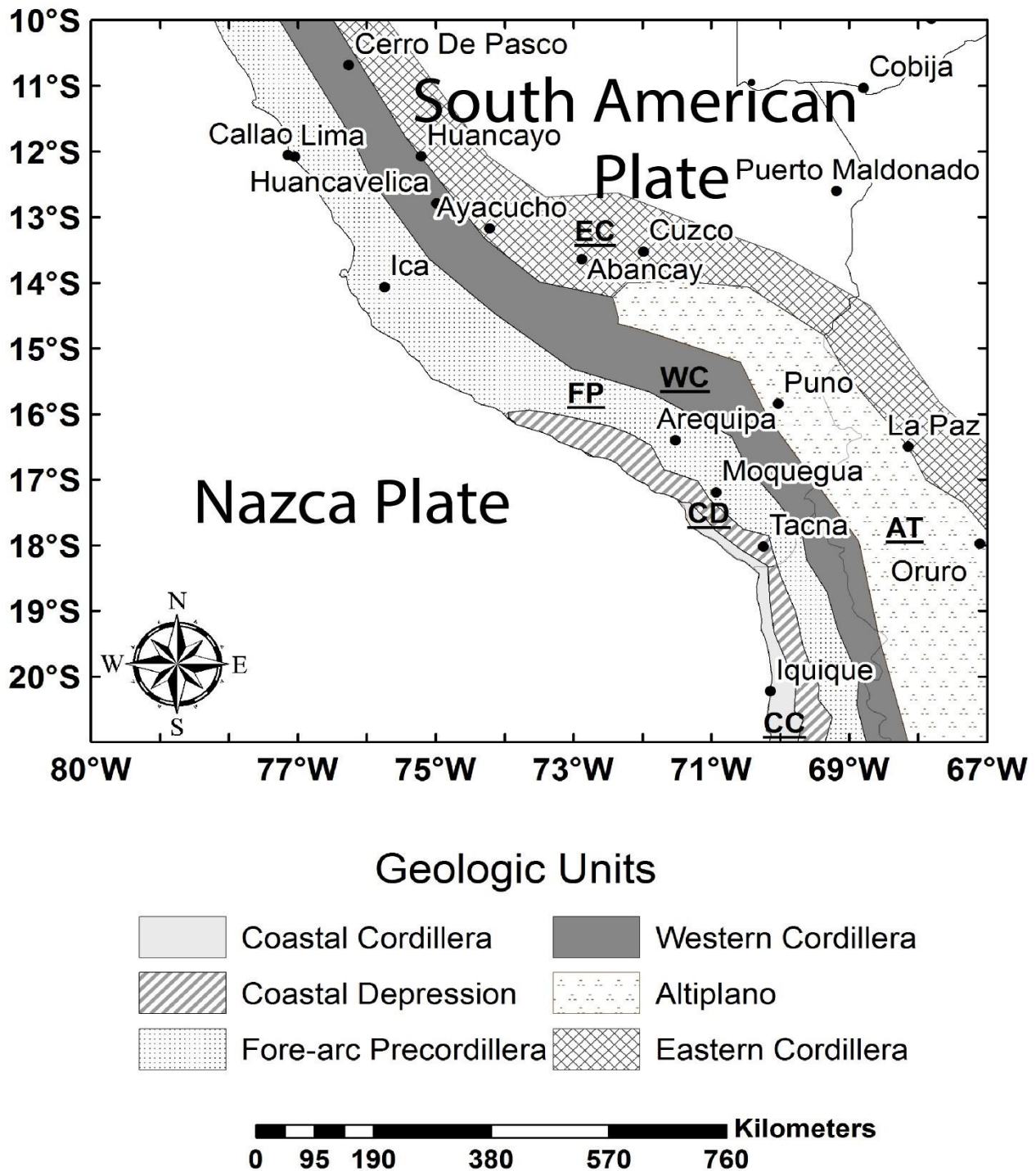


Figure 2. A geologic map of the Peru-Chile subduction zone highlighting the various geologic structures. Abbreviations: CC Coastal Cordillera, CD Coastal Depression, FP Fore-arc Precordillera, WC Western Cordillera, AT Altiplano, EC Eastern Cordillera (after Charrier et al., 2013).

3. GRAVITY DATABASE AND METHODOLOGY

To construct the 2.5-D gravity models of the central Andean subduction zone, I use the free air gravity anomaly data from the International Centre for Global Earth Models (ICGEM). These data are combined surface and satellite gravity field data from the EIGEN-6C4 (European Improved Gravity model of the Earth by New techniques) geopotential model (Förste et al., 2014). The EIGEN-6C4 model is a combination of land gravity data, altimetry over the oceans, EGM2008 (Earth Gravity Model; Pavlis et al., 2012), DTU 2'x2' global gravity anomaly grid (Danish Technical University; Andersen, 2010) and gravity data from three satellite missions (GOCE- Gravity Field and Steady-State Ocean Circulation Explorer, GRACE- Gravity Recovery and Climate Experiment, and LAGEOS- Laser Geometric Environmental Observation Survey). These data have a spatial resolution of Ca. 10 km and are based on the WGS84 (World Geodetic System) reference ellipsoid, thus allowing the development of a detailed representation of the subduction zone.

I applied standard gravity corrections to the free air gravity anomaly, and the reductions include Bouguer, terrain, and Boullard-B corrections. The Boullard B correction accounts for the curvature of the Earth. The Bouguer correction corrects for mass below the measurement point relative to the WGS84 reference ellipsoid. The terrain correction accounts for topographical effects around the measurement point within a 168 km radius. For the terrain correction, I used elevation data from the global relief model of the Earth's surface (ETOPO-1; Amante and Eakins, 2009). The standard reduction density for this study is 2670 kg m^{-3} . The 2.5D gravity

model was developed using GM-SYS Gravity and Magnetic Modelling software which makes use of Green's theorem to calculate the gravity anomalies of irregular structures.

3.1. Wavelength Filtering

Filtering is a useful tool for potential field analysis. Through filtering we can see structures that may not be as apparent when observing the total signal of the data. This is done by mathematically passing and omitting user determined wavelength ranges in wave number domain.

In this study two filters were applied to the Bouguer anomaly. The first is the low-pass or regional filter. To create this filter I selected a cut-off wavelength by iteratively increasing the cut-off until only regional features were shown. Since this step is a user based analysis, as the user determines when the features are regional, I also compared the resulting regional filter to an upward continuation filter. The upward continuation filter is another type of low-pass or regional filter in the sense that it takes the data and transforms it to appear as if it had been measured at various heights above the original measurement point. This process suppresses the short wavelength (shallow structures) and enhances the long wavelength (deep and regional structures). When both the upwards continuation and the long wavelength filter are similar then we have the desired cut-off wavelength.

The next filter is the high-pass or residual filter. This filter is achieved by suppressing the long wavelength and keeping the short wavelength. This can be achieved by both a high-pass filter and a downward continuation and thus followed the same sequence as described above for the low-pass or regional filter.

3.2. Isostasy Modelling

To evaluate the isostatic state of the central Andes I calculated the isostatic or expected topography and residual topography. The expected topography is the amount of topography that is capable of being isostatically supported when theoretically calculated using the Vennig-Meinnessz's isostatic model. The residual topography is a result of subtracting the observed from expected topography.

The Vennig-Meinnessz isostatic model was chosen because it incorporates total lithospheric support. If I had only chosen to use crustal support for the expected topography then I may have seen fictitious areas of the fore-arc that are unsupported. This could result in an analysis that indicates extra forces present to support the observed topography, thus resulting in these extra fictitious forces affecting the plate locking analysis. To avoid this I include total lithospheric support.

4. INITIAL MODEL & CONSTRAINTS

In this discussion I present six gravity models, representative of the Central Andes subduction zone. The density models show the crust and upper mantle structure of the convergent zone with varying tectonic settings, as seen in Figures 1 & 2. The models run along latitudinal lines, span an approximate distance of 9 km, and reach a maximum depth of 250 km. Two southern models, at 20°S & 19°S, represent the southern Peru and northern Chile subduction zones. The northern model, 16°S, is located in the flat slab region where the Nazca ridge subducts beneath the South American plate.

Within these models, major structures are constrained by previous studies using varying seismic velocity models and data. The Moho depth and Lithosphere-Asthenosphere Boundary (LAB), Ca. 40 km and 100 km respectively, have been defined by velocity models developed for the region (Gutscher et al., 2000; Husen et al., 2000; Yuan et al., 2000; Oncken et al., 2003; Comte et al., 2004; Krebbenhöft et al., 2004; Bilek 2010; Chulick et al., 2013; Kumar, 2015). Table 1 shows the P-wave velocities and densities of major structure in the Central Andes.

<i>Tectonic Units</i>	P-Wave Velocity (km s⁻¹)	Density (kg m⁻³)	References
<u><i>Continental Domain:</i></u>			
<i>Upper & Middle Crust</i>	5.0 – 7.0	2540 – 2970	Husen et al. (2000), Oncken et al. (2003), Krabbenhöff et al. (2004), Kumar (2015)
<i>Lower Crust</i>	6.7 – 7.3	2880 - 3060	Husen et al. (2000), Oncken et al. (2003), Kumar (2015)
<i>Continental Mantle Lithosphere</i>	7.6 – 8.2	3200 – 3330	Oncken et al. (2003), Kumar (2015)
<u><i>Oceanic Domain:</i></u>			
<i>Sediment</i>	2.0 – 5.5	1910 – 2650	Husen et al. (2000), Krabbenhöff et al. (2004)
<i>Oceanic Crust</i>	6.5 – 7.3	2830 – 3200	Krabbenhöff et al. (2004)
<i>Oceanic Mantle Lithosphere</i>	7.8 – 8.15	3220 – 3350	Norabuena and Snoke (1994), Krabbenhöff et al. (2004)
<i>Asthenosphere</i>	8.15	3350	Norabuena and Snoke (1994), Kumar (2015)

Table 1. Densities and P-wave velocities used in 2.5-D gravity modeling

The densities of major tectonic structures above the Moho are derived from P-wave velocities at relevant pressure and temperature conditions using the Sobolov and Babeyko, 1994, method. Sub-Moho structure density is calculated with the Nafe and Drake, 1957, method. The temperature used for density calculation is based on a subduction zone thermal model from Mahatsente and Ranalli in 2004. Additionally, a pressure gradient of 30 MPa/km is used for density determination. These two assumptions, temperature and pressure, can introduce error into the density determination. We see a negligible amount of error in Table 2, thus confirming that the assumptions are within acceptable range.

<i>Tectonic Units</i>	Density (kg m⁻³)	Variations (kg m⁻³)
<u><i>Continental Domain:</i></u>		
<i>Upper & Middle Crust</i>	2700 – 2940	18
<i>Lower Crust</i>	3100	15
<i>Continental Mantle Lithosphere</i>	3200	10
<u><i>Oceanic Domain:</i></u>		
<i>Sediment</i>	2550 - 2600	100
<i>Oceanic Crust</i>	2900 – 3250	25
<i>Oceanic Mantle Lithosphere</i>	3200 – 3365	5
<i>Asthenosphere</i>	3350	4

Table 2. Final densities used in 2.5-D gravity models and their uncertainty

The geometry and density of the subducting Nazca slab and the overriding South American plate are well defined by previous tomography and receiver function studies (Yuan et al., 2000; Gutscher et al., 2000; Oncken et al., 2003; Krabbenhöft et al. 2004., Comte et al., 2004; Kumar 2015). The oceanic and continental mantle lithospheres have velocity ranges of 7.8 – 8.15 km s⁻¹ and 7.6 – 8.1 km s⁻¹, respectively (Norabuena and Snoke, 1994; Oncken et al., 2003; Krabbenhöft et al., 2004; Kumar, 2015). The density of the asthenosphere is based on the P-wave velocity model (Norabuena and Snoke, 1994).

The oceanic and continental crustal density and geometry are obtained from seismic tomography (Husen et al., 2000; Oncken et al., 2003; Krabbenhöft et al., 2004; Kumar 2015). The P-wave velocity of the oceanic crust (6 – 8 km thickness) ranges from 6.5 – 7.3 km s⁻¹ (Oncken et al., 2003; Krabbenhöft et al., 2004). The P-wave velocity of the continental crust, which consists of 15 km upper crust and 25 km lower crust, ranges from 5.0 – 7.0 km s⁻¹ and 6.7 – 7.3 km s⁻¹, respectively (Husen et al., 2000; Oncken et al., 2003; Krabbenhöft et al., 2004; Kumar, 2015). The density and thickness of the sediment are derived from the P-wave velocity, 2.0 – 4.5 km s⁻¹, of wide-angle seismic reflection (Husen et al., 2000; Krabbenhöft et al., 2004).

5. RESULTS AND DISCUSSION

5.1. Gravity Anomaly Analysis

The Bouguer anomaly, shown in Figure 3, indicates significant differences between the ocean (Ca. 440 mGal) and continent (Ca. -350 mGal). In addition to gravity differences, there is also an inverse relationship between topography and anomaly. A positive elevation correlates with a negative Bouguer anomaly, whereas a negative elevation correlates with a positive anomaly. This correlation is expected because the Bouguer anomaly is directly related to the density distribution in the crust. The Bouguer anomaly over the western and eastern cordillera, where the maximum elevation and average crustal root depth are 6.3 km and 50 km, respectively, is in the order of -475 mGal. The Bouguer anomaly decreases away from the cordillera, a result of the absence of a crustal root. Towards the coast, the elevation approaches sea-level and the anomaly reaches a value of 0 mGal. Within the ocean, the elevation decreases to a maximum of 7.6 km depth in the trench. The dense Nazca Plate and shallower mantle result in a maximum Bouguer anomaly of 541 mGal. Within this region, the Nazca ridge, Ca. 250 mGal, is a prominent feature seen in the Bouguer anomaly. This is a result of the Nazca ridge being less dense than the surrounding oceanic crust. In addition to the change in density, the Nazca ridge also reaches a maximum thickness of 18 km, far larger than the average 6 km thickness of the surrounding oceanic crust (Woods and Okal, 1994). The change in density and thickness is a product of the Nazca ridge being an extinct spreading center and having an age of 31 ± 1 Ma at the trench (Ray et al., 2012).

To further analyze the signal content of the Bouguer anomaly, I applied upward continuation and wavelength filtering. The upward continuation was applied at heights ranging from 10-100 km. I chose a final height of 50 km because it effectively showed regional structures. I then applied a regional filter with a cut off wavelength of 290 km. This wavelength effectively removed the small structure signatures in the data, thus leaving the regional features. The results of the upward continuation and low pass filter were compared to select the cut off wavelength. Each showed similar amplitude, thus indicating a regional structure map.

The regional gravity map, Figure 4A, shows a large continuous negative anomaly, - 350 mGal, over the cordilleras. This negative anomaly represents the low-density crustal root of the cordilleras. The other key structure that can be seen in the regional gravity map is the Nazca ridge. The ridge has an average anomaly of 250 mGal and is surrounded by an oceanic crust that is on average 300 mGal. The residual gravity map (Figure 4B), which is the result of high pass filter, shows the gravity signal of the shallow structures in the region. There are positive anomalies in a parallel trend with the cordilleras. Some of these positive anomalies correlate with volcanic centers in the region.

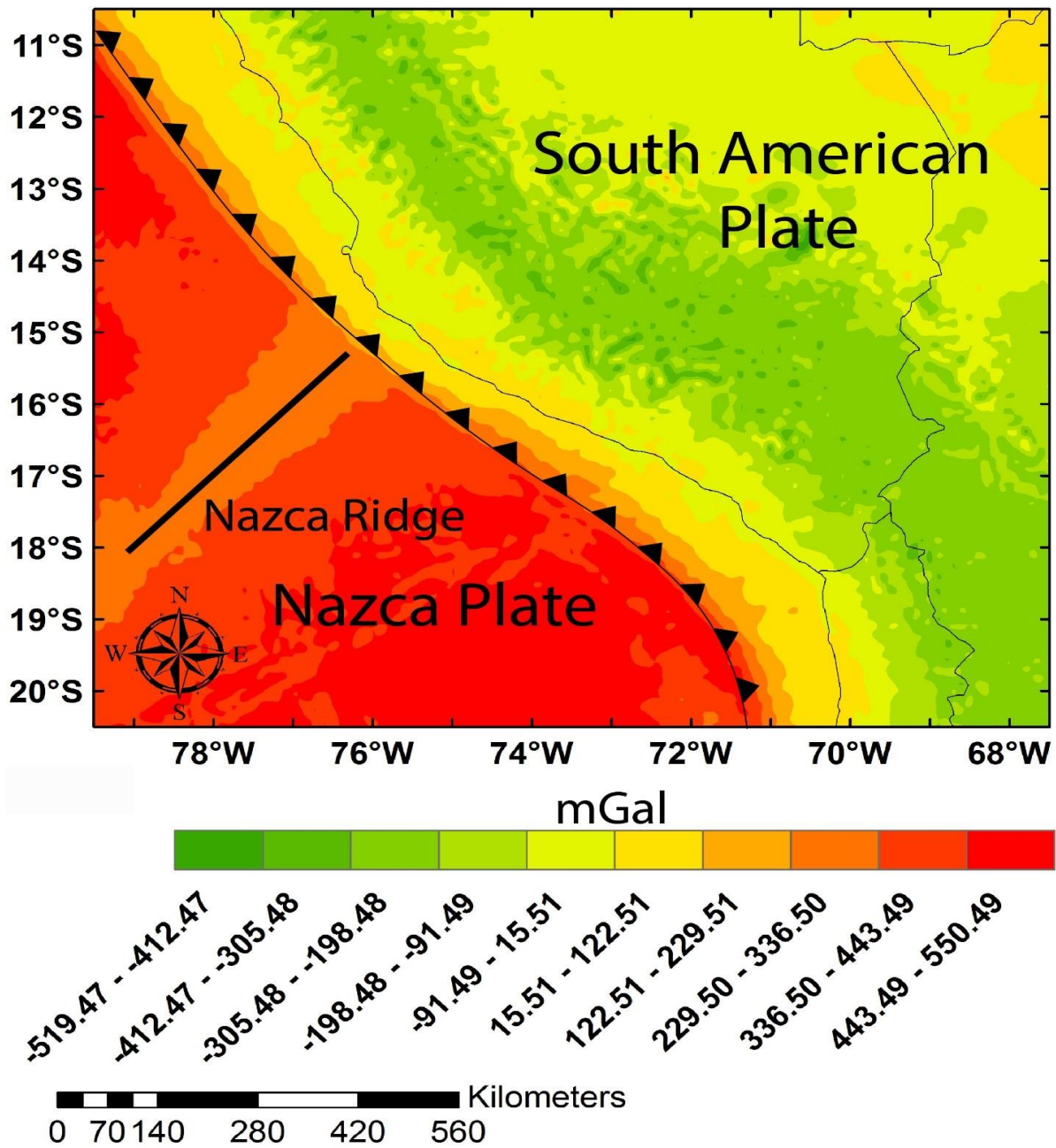
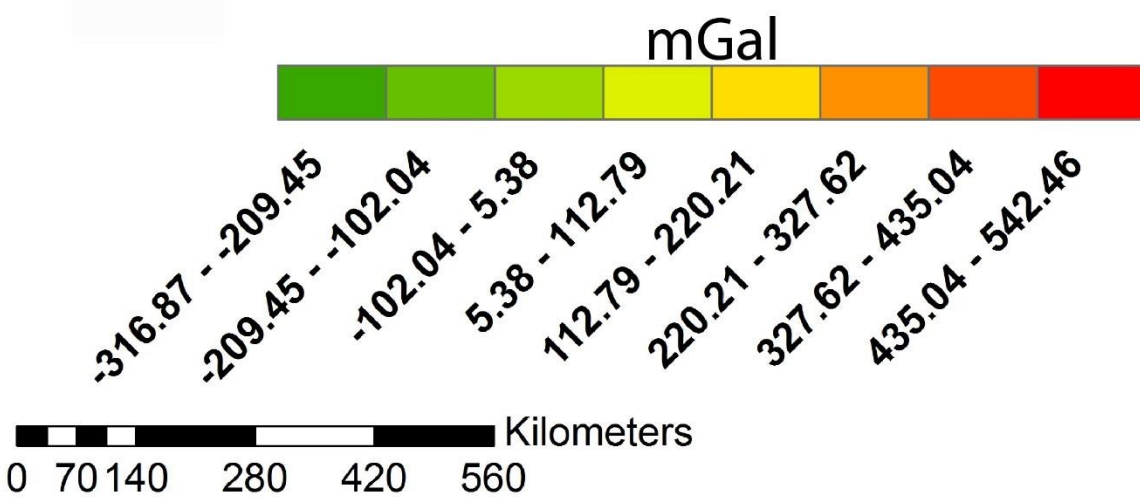
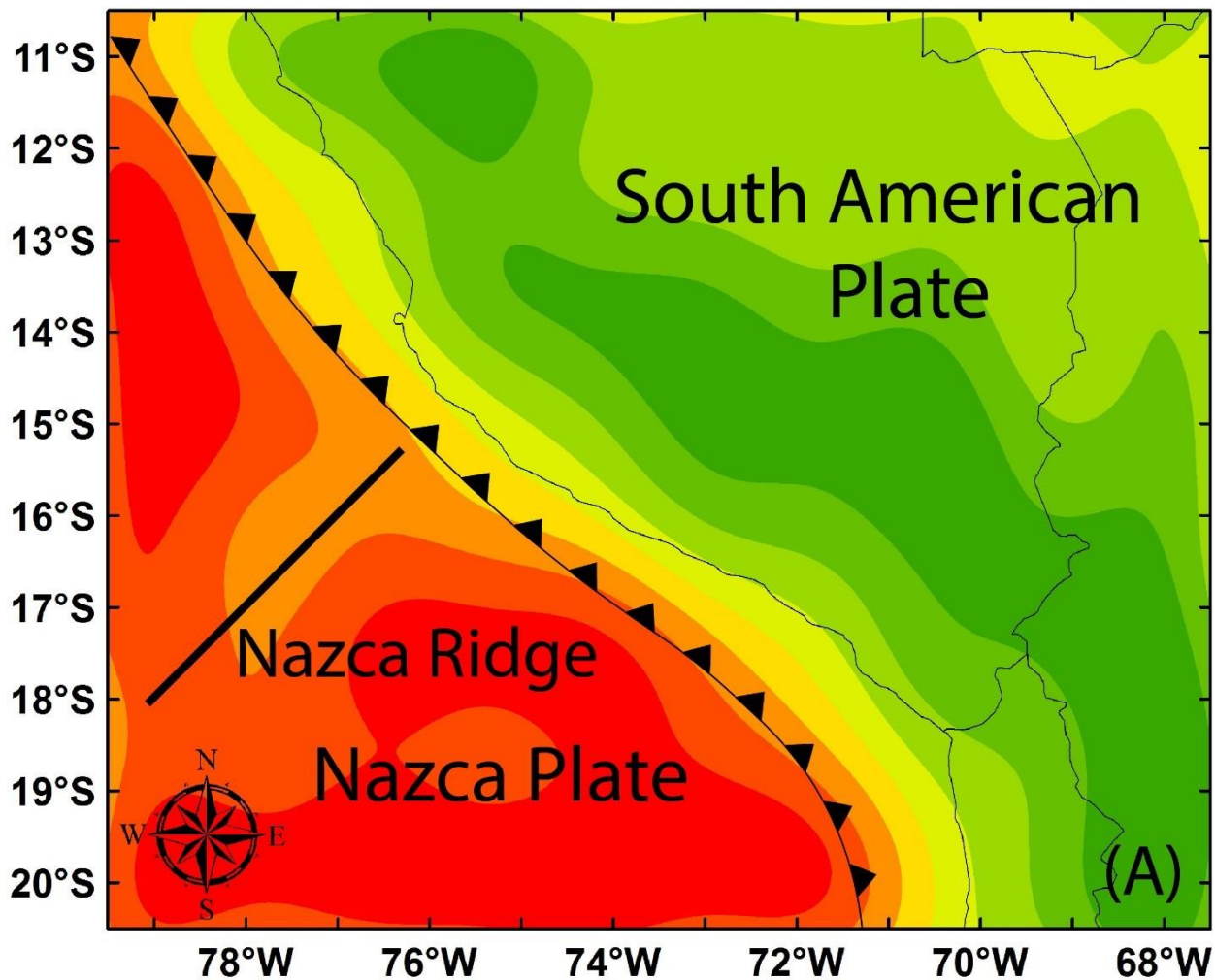


Figure 3. A complete Bouguer Anomaly map of the Peru-Chile subduction zone. The saw tooth line is the location of the trench and the straight line is the Nazca Ridge.



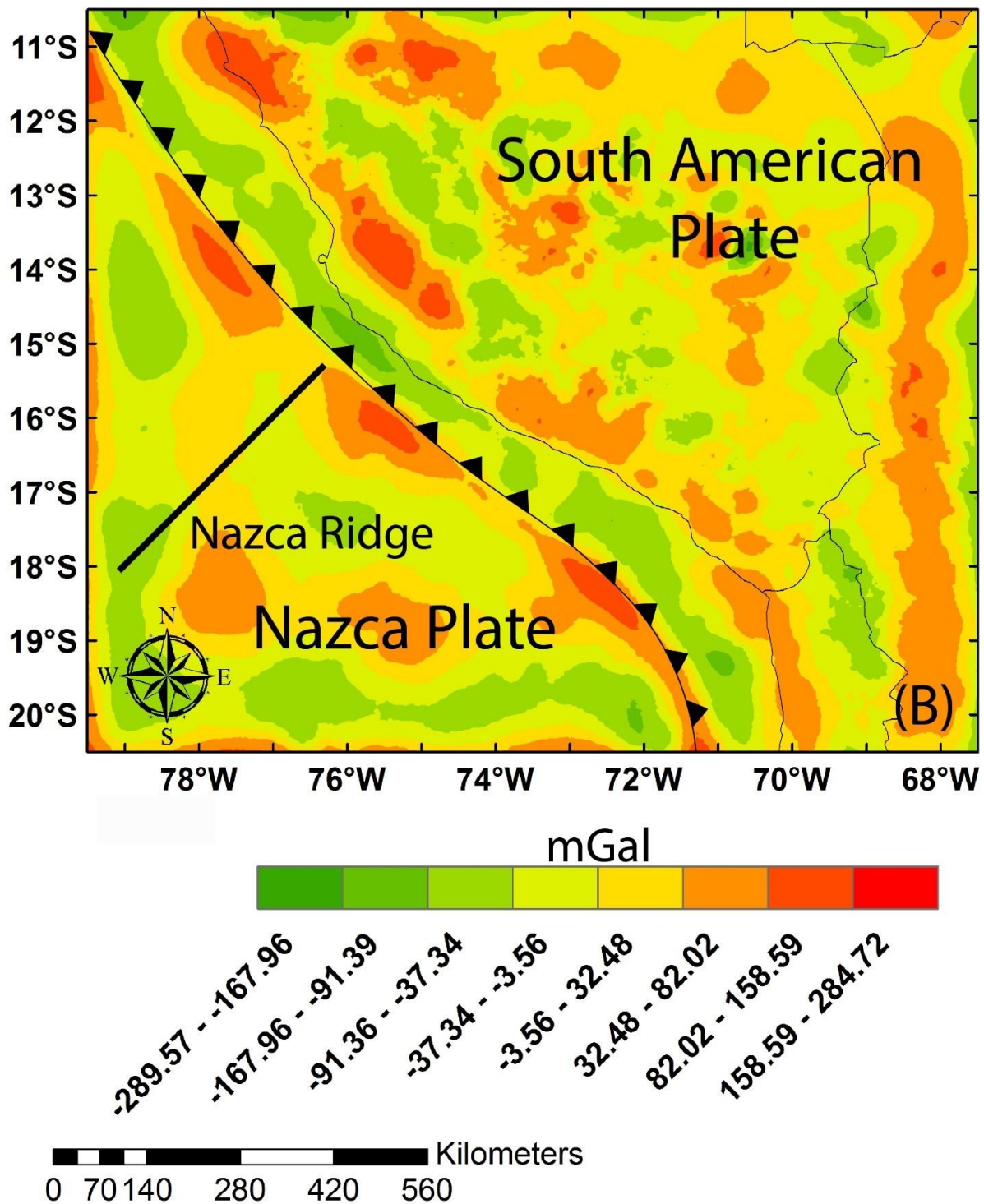


Figure 4. (A) Regional Bouguer anomaly shows the large-scale structures. The crustal root is seen as the long negative anomaly trending NW-SE. (B) Residual Bouguer anomaly shows shallow structures. These anomalies can be attributed to volcanic centers and cordilleras.

5.2. Lithospheric Structure & Locking Mechanism

Geodetic data indicates a highly coupled plate interface between the subducting Nazca and overriding South American plates beneath the Central Andes subduction zone. I have developed six models in the Central Andes to explore the effects of the fore-arc structures on plate coupling. I use these models to evaluate our hypothesis of high-density structures causing a downward buoyancy force that effectively locks the Nazca and South American plates.

The first two models shown in Figure 5 A & B, are located in the southern seismic gap. In this region of north Chile, the slab is subducting at a relatively steep angle, Ca. 30° . The location of the slab is constrained by available earthquake data within 0.1 degrees north and south of the profile.

Both models show a high-density structure (2940 kg m^{-3}) in the fore-arc, which is higher than the average density of continental crust. The high-density fore-arc structure could be batholith or ophiolite. Within the study area, there is a collection of middle to late cretaceous granodiorite and tonalite rock units, known as the Andean batholith (Gunnell et al., 2010). Previous studies have found indication of batholithic and ophiolitic units within the Colombian Andes (Jaramillo et al., 2017). In the southern Andes ophiolitic complexes of early Cretaceous have been thrust on top of continental units during orogenic processes (Curtis et al., 2010; Calderón et al., 2012). This high-density structure could provide enough of a downward force to effectively lock the plate interfaces.

To determine the lithostatic load variations in the fore-arc, I calculated vertical stress anomalies on top of the subducting Nazca slab along East-West transect based on density model (Figure 6). The vertical stress anomalies are determined relative to a reference lithospheric column, representing the average continental crust and upper mantle. The reference lithospheric

column consists of 15 km thick upper crust, 20 km thick lower crust, and lithospheric mantle. The densities of the reference upper crust, lower crust and lithospheric mantle are 2670, 2900, 3350 kg m⁻³, respectively. The vertical stress anomaly, resulting from the high-density fore arc structure, on top of the subducting Nazca plate (Figure 5 A & B), ranges from 20 – 40 MPa (Figure 6). This is significantly higher than the pressure exerted on average continental lithosphere at the same depths. Thus, the high-density fore-arc structure may be exerting extra pressure on the subducting Nazca slab and thereby locking the plate interfaces.

Additionally, the mantle wedge, resulting from subduction, has the potential to experience small scale convection. The small-scale convection in the mantle wedge can provide strong enough forces to help inhibit the motion of the subducting Nazca plate. The forces provided by these two features, small scale convection in the mantle wedge and high-density structures, could effectively lock the subducting Nazca Plate.

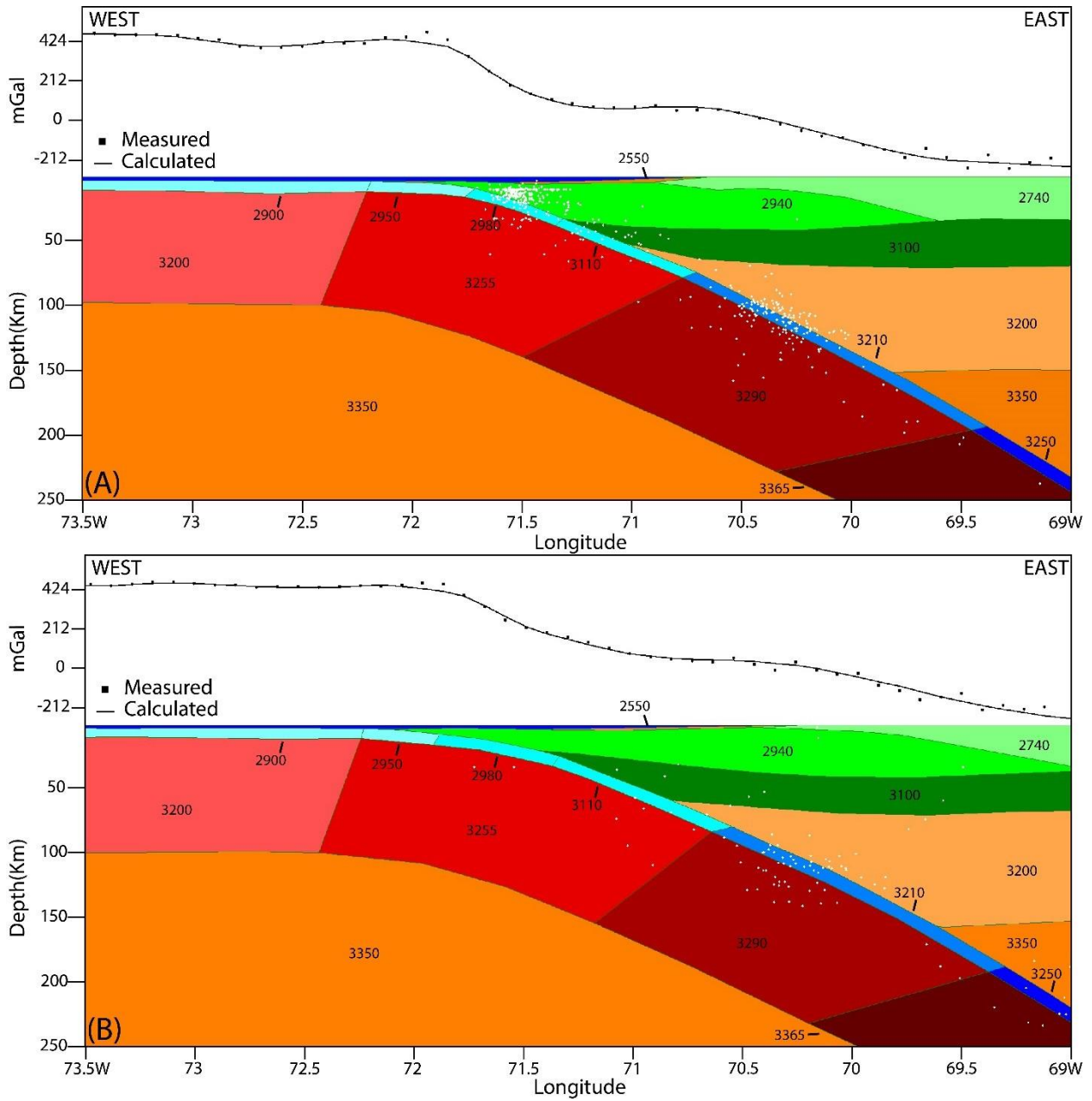


Figure 5. 2.5-D gravity model of the central Andes subduction at (A) 20° S and (B) 19° S. The two models located within the southern seismic gap zone. Numbers indicate densities of structures in kg m⁻³. White dots are earthquake hypocenters from the USGS database from 1960 - 2019.

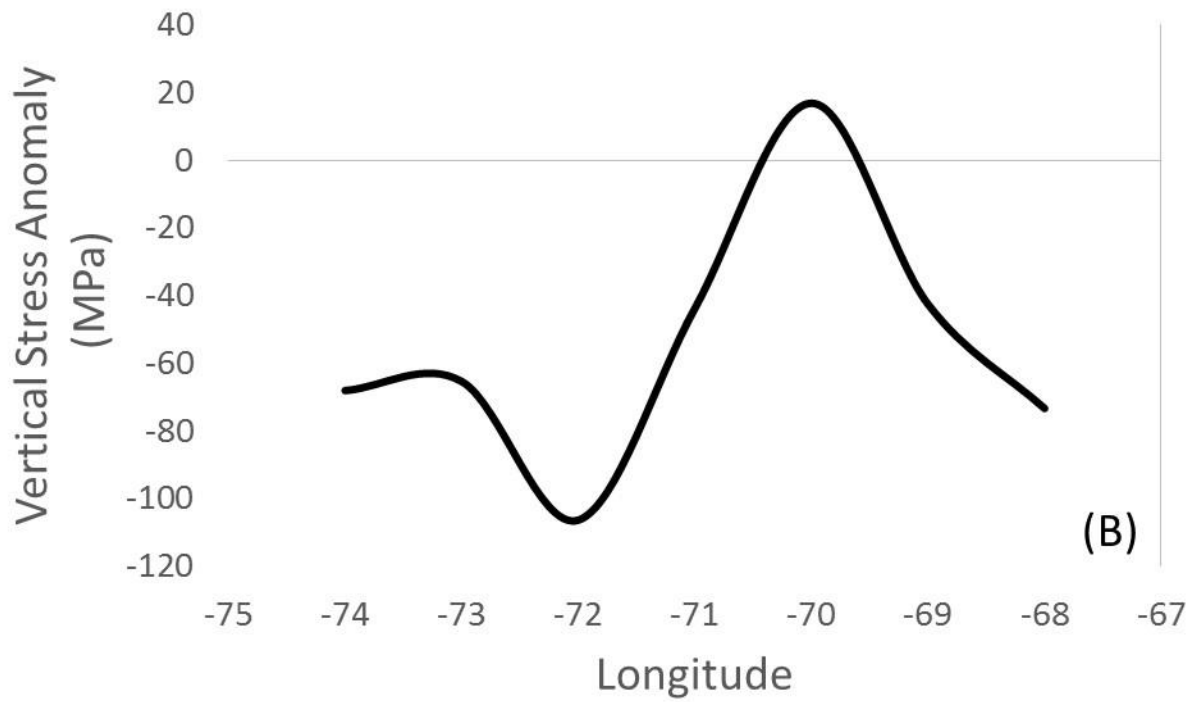
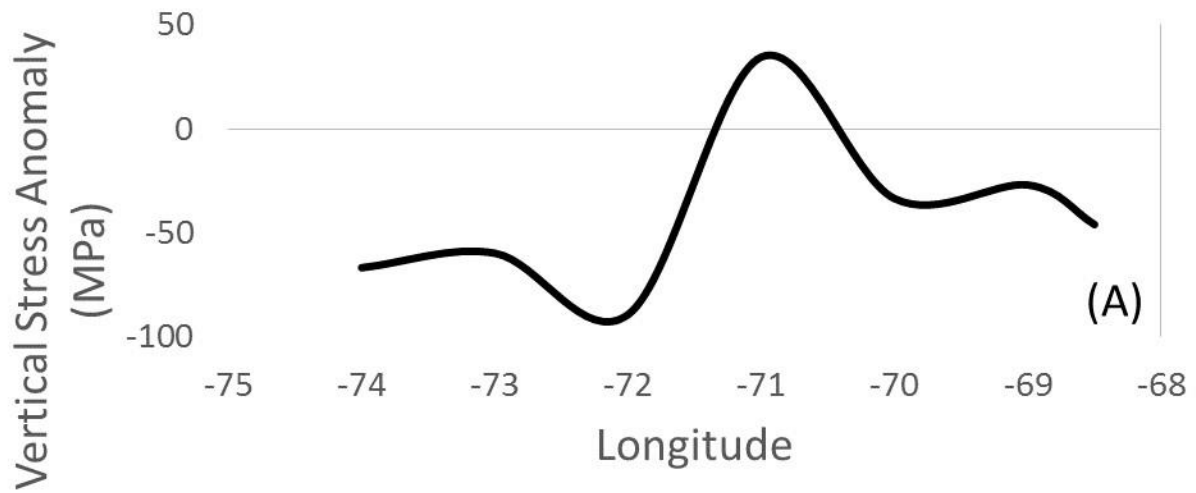


Figure 6. Vertical stress anomaly calculated on top of the subducting Nazca plate. **(A)** at 20°S **(B)** at 19°S.

As we move north, out of the seismic gap, our next model, Figure 7, is located where the Nazca ridge subducts beneath South America. The origin of the Nazca Ridge (NR) has been a subject of past contention. According to a geochronology study by Ray et al. (2012), the NR is a trail of volcanoes that are related to a hotspot currently near Salas y Gomez Island, far to the west. The NR is related to the Eastern Seamount Chain (ESC) in that they are both a result of the hotspot. It is thought that when the NR changes into the ESC, Ca. 23 Ma, this signifies the breakup of the Farallon plate (Barckhausen et al., 2008; Ray et al., 2012).

This location has similar densities for the crust and mantle as the two southern models. One stark difference within the crust, is the absence of a high-density structure. Contrary to the south, previous studies indicate a shallow, less than 25 km, slow velocity (low-density) structure (Kumar, 2015). Even with the absence of a high-density structure, GPS data still indicates that the plates in this region are coupled (Figure 9, Chlieh et al., 2011).

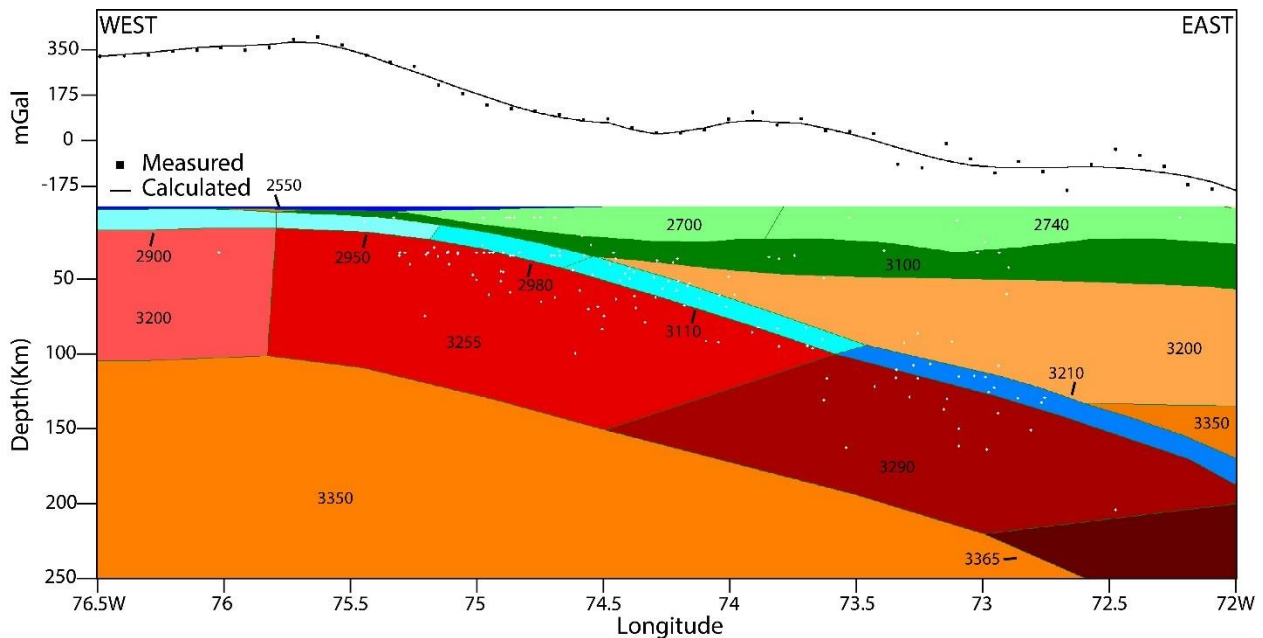


Figure 7. 2.5-D gravity model of the central Andes subduction at 16°S, a loosely coupled region. Numbers indicate densities of structures in kg m^{-3} . White dots are earthquake hypocenters from the USGS database (events from 1960 – 2019).

The plate coupling in this region can be attributed to the subducting Nazca Ridge. The low-density material of the ridge causes the subducting Nazca slab to experience an upwards buoyancy force, counteracting the downward thermal buoyancy force and pulling the slab upward into the South American plate (Figure 7). The vertical stress anomaly on the subducting Nazca plate that is caused by the low-density ridge can be seen in Figure 8. A vertical stress anomaly of Ca. 15 MPa is the least amount of stress among the three models, agreeing with the lesser coupling coefficient value seen for this region in Figure 9.

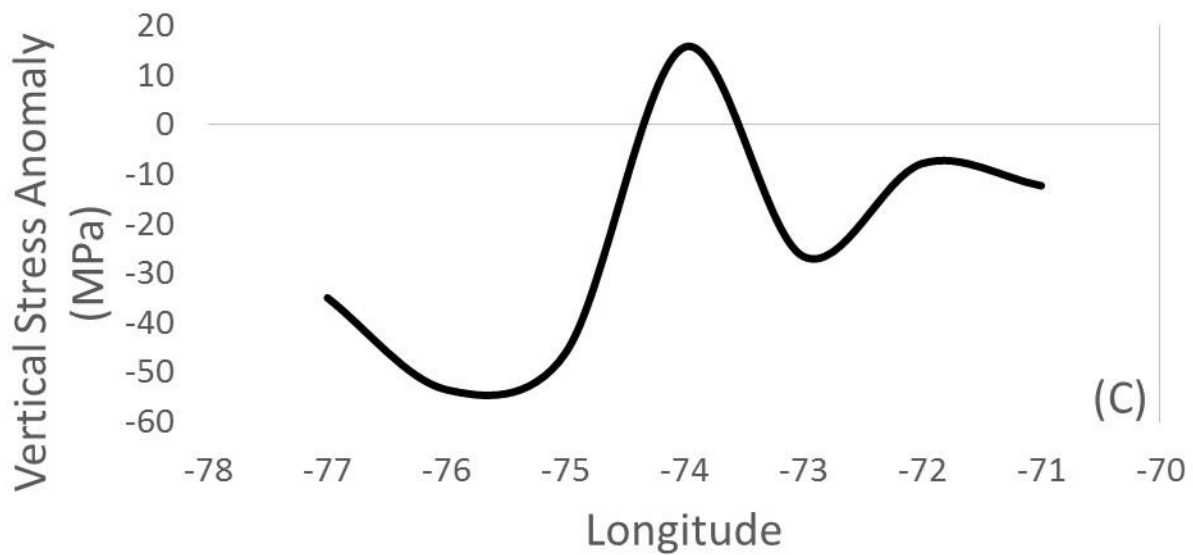


Figure 8. Vertical stress anomaly calculated on top of the subducting Nazca plate 16°S.

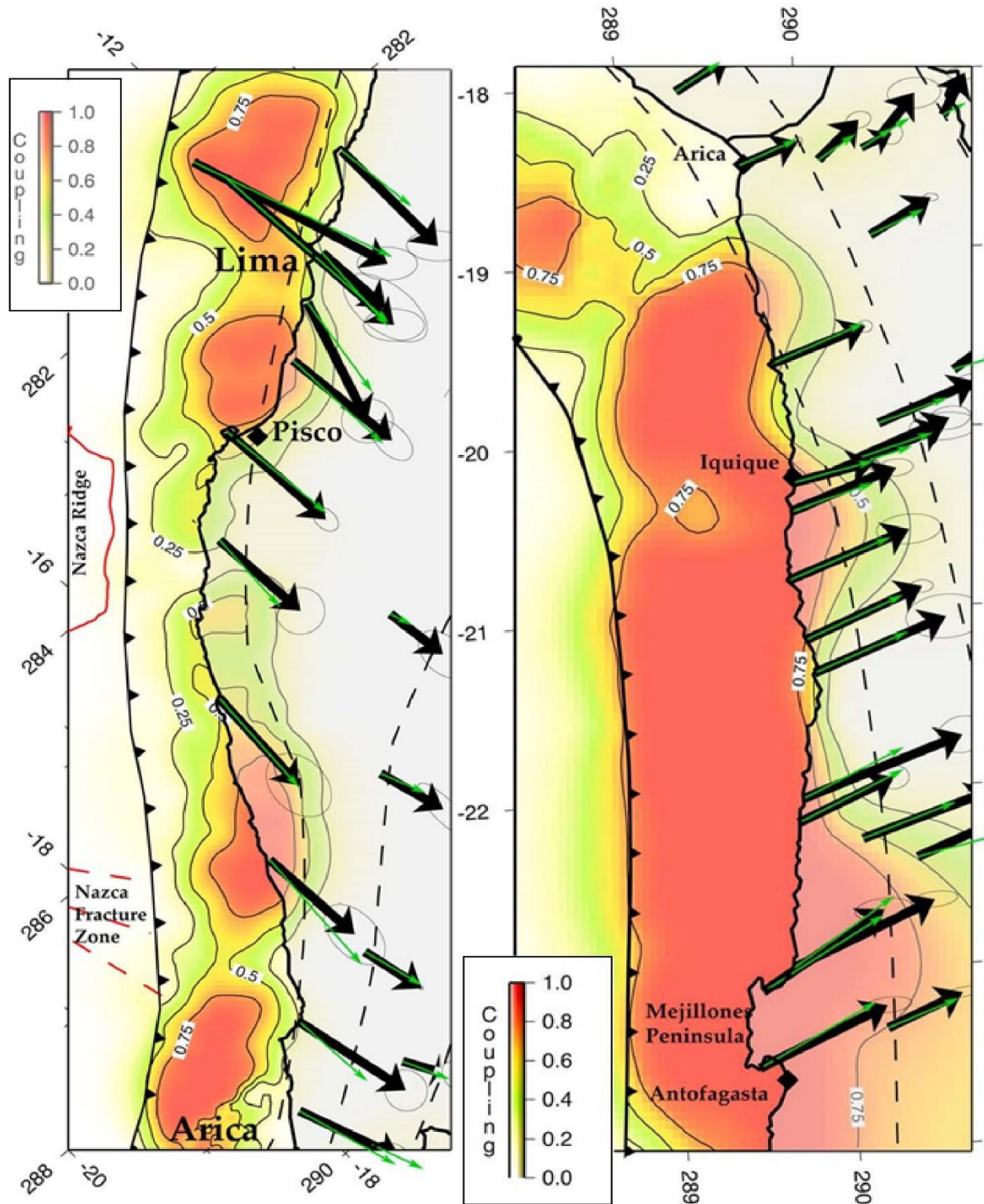


Figure 9. GPS derived coupling coefficients for the **(Left) Peru (Right) Chile** subduction zone. (Chlieh et al., 2011). The black and green arrows are observed and predicted interseismic GPS displacements, respectively.

To see a complete picture of how the subducting Nazca ridge affects the slab angle, a model at 12°S was developed (Figure 10). At this location the Nazca ridge crosses the East-West models obliquely. The ridge resides about 4° East of the trench within the subducting Nazca slab, thus reducing the subduction angle to Ca. 20° within this region, as seen in Figure 10. The coupling within this region, centered around Lima, Peru, is Ca. 0.5, as seen in Figure 9, and it can be explained by the Nazca ridge producing a positive buoyancy force and pinching against the Fore-arc. This is similar to the model at 16°S and contrary to 20°S & 19°S, where the coupling is explained by a high-density Fore-arc structure.

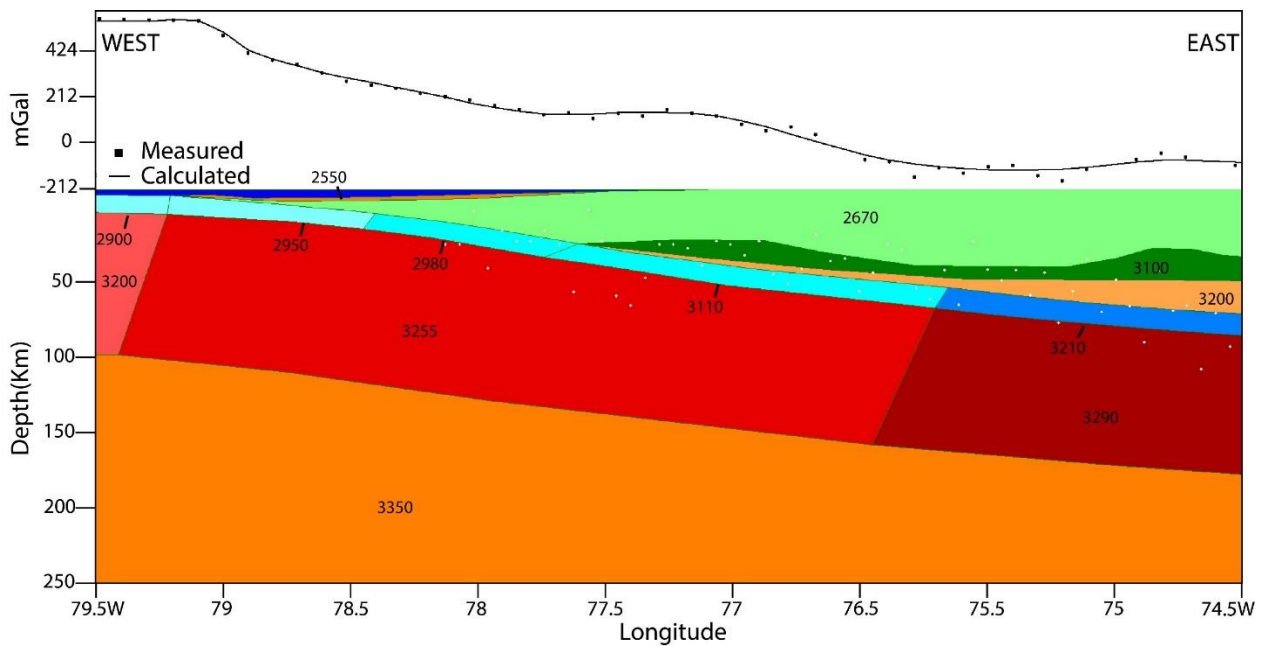


Figure 10. 2.5-D gravity model of the central Andes subduction at 12°S, a loosely coupled region. Numbers indicate densities of structures in kg m^{-3} . White dots are earthquake hypocenters from the USGS database (events from 1960 – 2019).

In addition to developing East-West (Latitudinal) models, I have developed two North-South (Longitudinal) models. The purpose of these models was to analyze the longitudinal extent of structures seen within the latitudinal models, and to provide a constraint on the 3-D slab image that was developed.

The first model, at 69°W, was chosen because it resides within the Fore-arc and crosses the high-density structure seen around 20°S & 19°S. Within this model, Figure 11, we can see the high-density structure extends through 19°S, and ends just before 20°S. This indicates that at 20°S, the high-density structure is closer to the coast than 69°W, as is confirmed within the 20°S model, Figure 5A. The northern extent, Ca. 19°S, of the structure can also be seen within Figure 11. Once again, around 19°S, the structure is about to end, and when compared to the 19°S model, Figure 5B, the Fore-arc structure is closer to the trench.

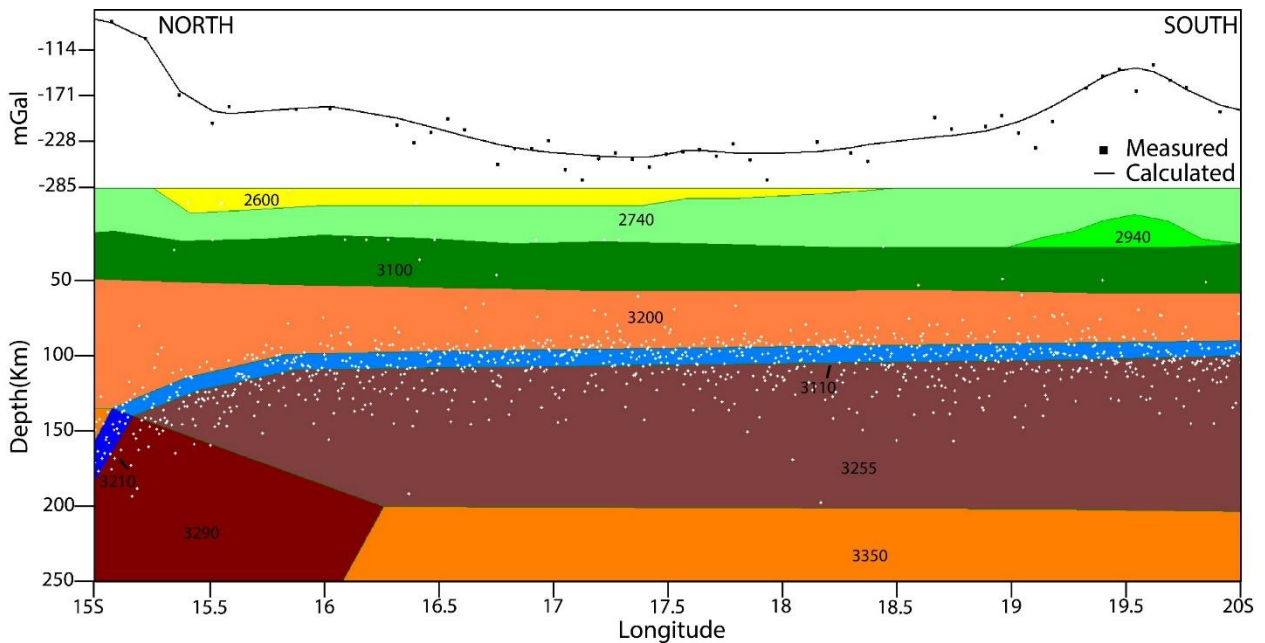


Figure 11. 2.5-D gravity model of the central Andes subduction at 69°W. Numbers indicate densities of structures in kg m^{-3} . White dots are earthquake hypocenters from the USGS database (events from 1960 – 2019).

The next longitudinal model that was developed, is centered on 75.5°W. This location was chosen for its proximity to the subducting Nazca ridge. Within this model, Figure 12, we can see that the Nazca ridge is prominent underneath the Fore-arc, around 12.5°S - 16°S. The positive buoyancy force, due to a thick, less dense ridge, has significantly flattened out the slab within this region. In addition to seeing the effects of the Nazca ridge, we can also see the density

segmentation of the Peruvian Fore-arc. This segmentation is extremely important because varying buoyancy forces in the region will affect the plate coupling, thus the asperity generation.

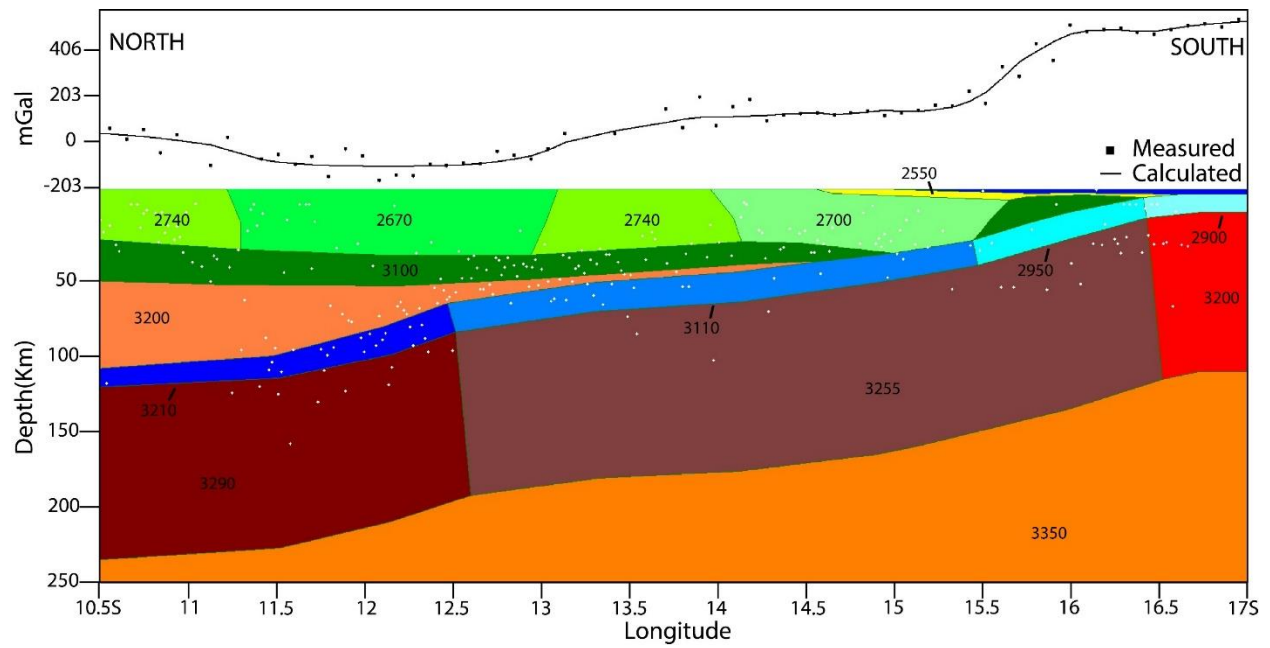


Figure 12. 2.5-D gravity model of the central Andes subduction at 75.5°W. Numbers indicate densities of structures in kg m⁻³. White dots are earthquake hypocenters from the USGS database (events from 1960 – 2019).

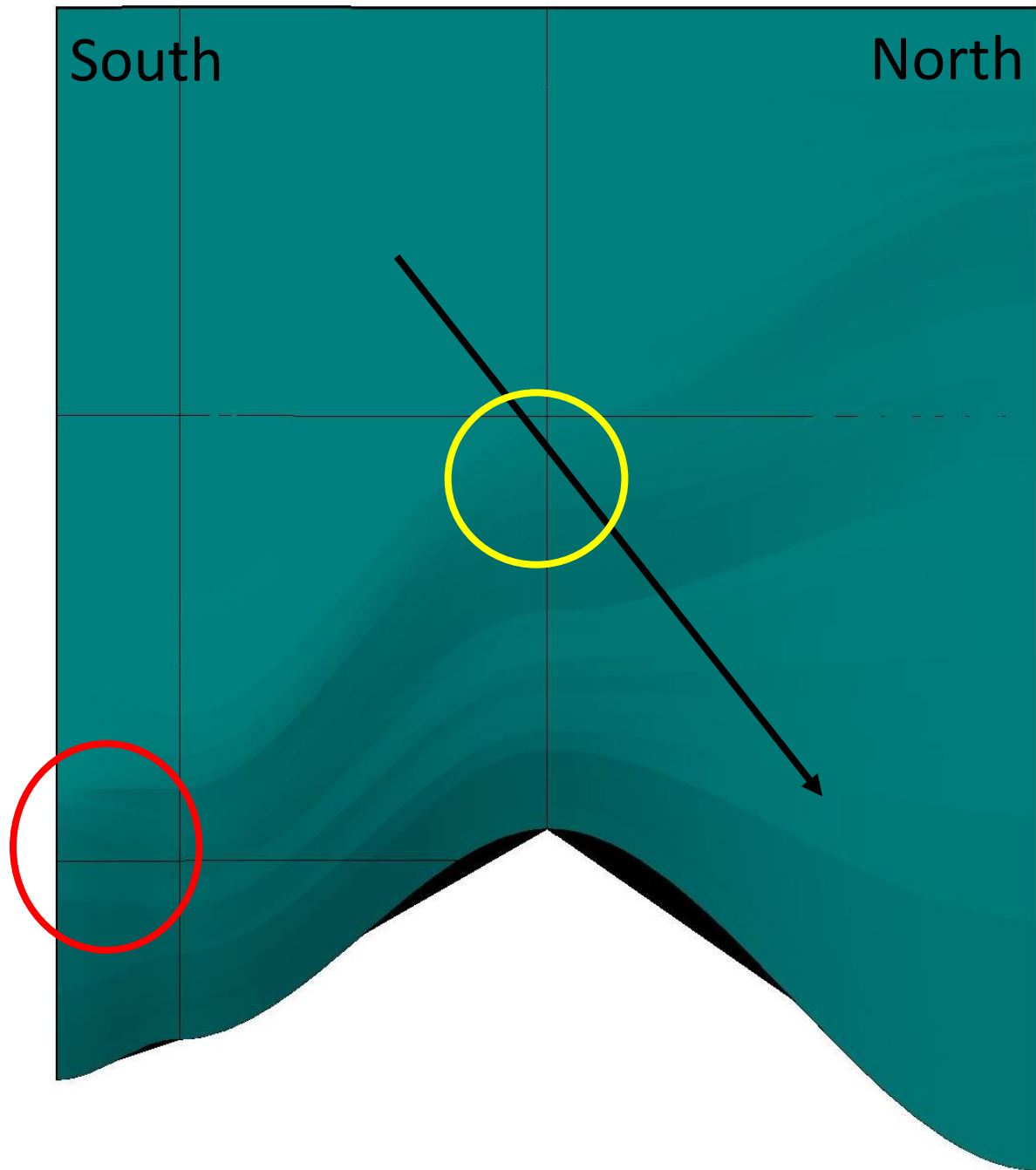


Figure 13. A map view of the subducting Nazca Slab. The red circle indicates approximate area of coupling due to the high-density structure. The yellow circle indicates approximate area of coupling due to the low-density Nazca ridge. The black arrow is the projection of the incoming Nazca ridge.

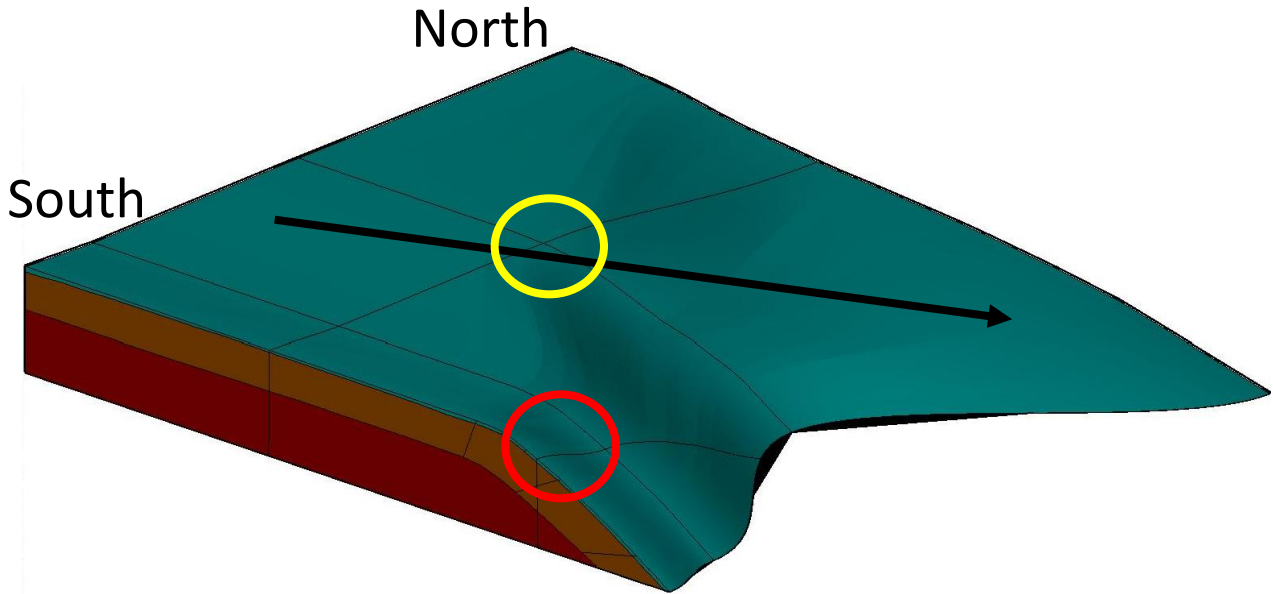


Figure 14. A South-East to North-West view of the subducting Nazca slab. The red circle indicates approximate area of coupling due to the high-density structure. The yellow circle indicates approximate area of coupling due to the low-density Nazca ridge. The black arrow is the projection of the incoming Nazca ridge.

The effects of the high-density fore-arc structure and Nazca ridge on plate coupling can be seen on the Nazca slab in 3-D (Figures 13 & 14). The high-density structure is pressuring the Nazca slab where it is steepest, Ca. 30° . Opposite of the high-density fore-arc structure, the low-density Nazca ridge pulls up against the fore-arc and causes coupling, the yellow circle in Figures 13 & 14. The yellow circle is the approximate location of where the Nazca ridge intersects the trench and then subducts in a North-Easterly direction, the black arrow. The northern extent of the slab is extremely flat, compared to the southern extent. This is a result of the subducted Nazca ridge being less dense and flattening the slab.

The coupling in both seismic gaps, the Peru-Chile border ($18^\circ\text{S}, 71^\circ\text{W}$) to ($21^\circ\text{S}, 71^\circ\text{W}$) and northern Peru ($1^\circ\text{S}, 81^\circ\text{W}$) to ($11^\circ\text{S}, 79^\circ\text{W}$), can be attributed to density anomalies in the crustal structure of the fore-arc and or the subducting Nazca slab. In the south, a high-density structure in the overlying fore-arc produces a downwards buoyancy force that effectively locks

the plates together. Opposite of this, a low-density structure in the north, Nazca ridge, in the oceanic crust produces an upwards buoyancy force. Thus, the trench parallel segmentation of the overriding South American and Nazca plates (density and crustal thickness variations) may control plate coupling and asperity generation in the Central Andes.

In comparison to the Central Andes seismic gaps, a major seismic gap known as the “Central Kuril Gap” is located on the Kuril-Kamchatka trench. This gap has experienced multiple large earthquakes in the last 20 years, namely the 2006 M_w 8.3 and 2007 M_w 8.1. The region is still considered to be highly coupled and has the potential to experience another megathrust earthquake (Baranov et al., 2015; Proshkina et al., 2017). According to Baranov et al. (2015), the fore-arc of the Central Kuril Islands is segmented into various tectonic units. This is supported by new evidence of intrusive massifs throughout the seismic gap (Proshkina et al., 2017). These massifs could be similar to that of the high-density structure seen in the Central Andes seismic gap. Thus, hinting at the cause of the Kuril gap, which was not distinguished in previous studies.

5.3. Isostatic State of central Andes

The continental margin is characterized by recent active volcanism related to volcanic arcs (e.g. Western Cordillera). There is growing evidence of low-velocity zones below the western margin of the Peru Chile subduction zone caused by deep crustal magmatic reservoirs. This is attributed to partial melting occurring at a depth of 20-60 km (Wigger et al., 1994; Echernacht et al., 1997; Schilling et al., 1997). The effects of low-velocity zones associated with magma chambers and small-scale convection cell in the mantle wedge on the overall isostatic compensation in the fore-arc of the Central Andes are not well understood. To assess the isostatic state of the Central Andes, I determined residual topography (difference between observed and

isostatic topography) using elevation and crustal thickness models. The elevation dataset is the ETOPO-1 Global Relief Model (Amante & Eakins, 2009) and the crustal thickness model is the LITHO 1.0 model (Pasyanos et al., 2014). The computation of isostatic topography is based on the Vennig-Meinesz's isostatic model and includes crustal and mantle support (Figure 15, Vennig-Meinesz, 1939).

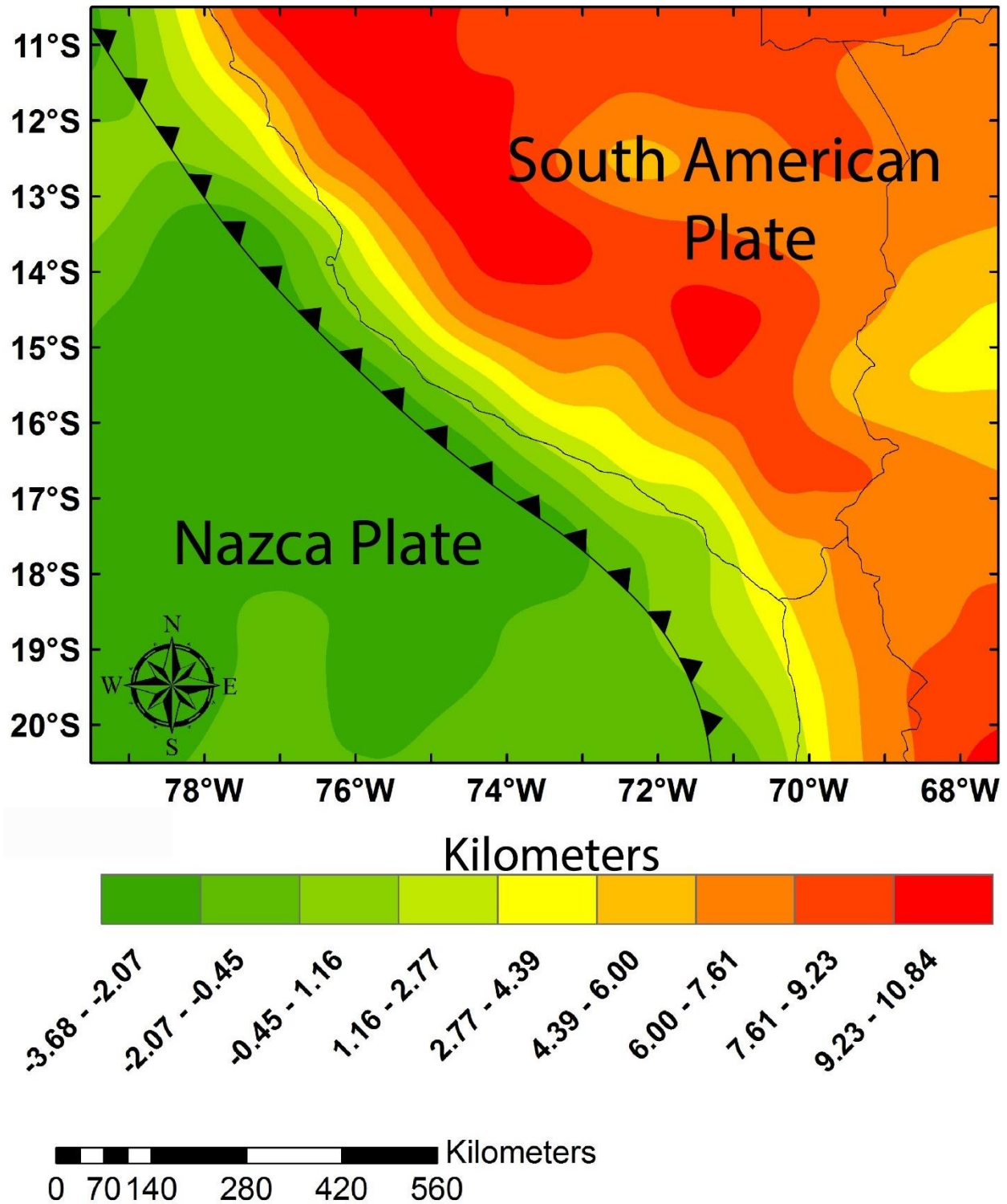


Figure 15. Isostatic topography of the Central Andes based on the Vennig-Meinesz, 1939, model. The saw tooth line indicates position of the trench.

The Nazca plate and the western part of the Central Andes are characterized by positive residual topography (Ca. 0.78) Figure 16, indicating that the two regions may not be isostatically supported. Our analysis indicates that the crustal thickness beneath the western part of the Central Andes may not be sufficient to isostatically support the observed topography. The western part of the central Andes may be partly supported by small-scale convection cell in the mantle wedge.

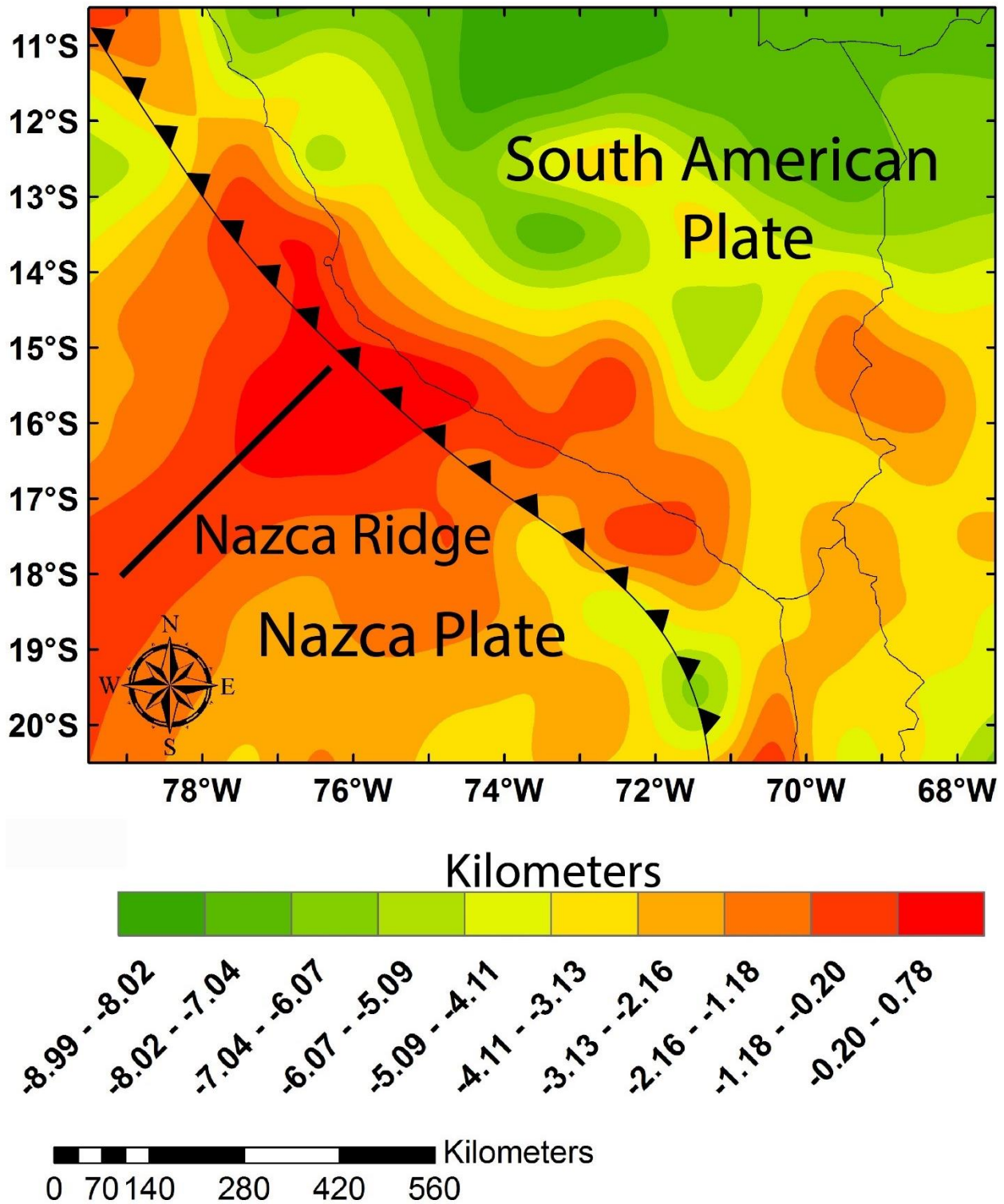


Figure 16. Residual topography of the Central Andes. The saw tooth line indicates location of the trench and the straight line is the Nazca Ridge.

The extra topography in the Nazca ridge may be attributed to extra forces present in the subducting oceanic lithosphere. One such force could be the result of drastic density changes in the subducting Nazca slab. The highly dense subducted Nazca slab, Ca. 3365 kg m^{-3} at Ca. 210 km depth, has a significant downward pull. Opposite of this, the now subducting Nazca Ridge is less dense than surrounding oceanic crust, due to the younger age, and has an upwards buoyancy force. These two forces, acting opposite of each other, effectively work in unison to raise the ridge and west-central Fore-arc to current day elevation. The Nazca Ridge is an ancient spreading center that is no longer active. According to basalt ages calculated by Ray et al., 2012, the ridge is roughly $31 \pm 1 \text{ Ma}$ at the trench.

The present estimate of residual topography for the Nazca ridge (Ca. 0.78 km) is higher than the previously predicted value for the ocean floor based on a global model (0.3 km; Steinberger et al. 2017). A 0.428 km difference between our study and the global model can be explained by the data sets used. The global model uses data from the CRUST 1.0 model (Laske et al., 2013) whereas our model utilizes the updated LITHO 1.0 model (Pasyanos et al., 2014). The updated LITHO 1.0 model incorporates the CRUST 1.0 model parameters and furthers the accuracy by fitting high frequency surface wave dispersion maps (Pasyanos et al., 2014)

6. CONCLUSIONS

The most recent major earthquakes in the Central Andes (Iquique 2014, $M_w=8.2$ and Illapel 2015, $M_w=8.3$) did not break the entire seismic gap as previously predicted. The plate interface in the seismic gap zone is still highly coupled. The seismic gaps are thought to be the location of the next megathrust earthquake. To understand what is causing these seismic gaps and assess locking mechanism of plate interfaces, I developed 2.5-D gravity models of the Central Andes subduction zone.

The gravity models in the seismic gap zone (at 20° S and 19° S) indicate the presence of a high-density (2940 kg m^{-3}) structure, which is higher than the average density of continental crust. This high-density fore-arc structure may be providing a downward force and locking the plate interface within a major seismic gap zone (18° S, 71° W) to (21° S, 71° W). Outside of this major seismic gap zone the gravity model (at 16° S) is lacking in a high-density structure but incorporates the subducting Nazca ridge. The effect of the low-density Nazca ridge is opposite in the sense that the structure reduces the negative thermal buoyancy force of the slab and thereby locks the plate interface. Thus, the trench parallel segmentation of the overriding and subducting plates (crustal thickness and density variations) may be one of the major controlling factors of plate coupling and asperity generation within the Central Andes.

In addition to exploring the lithospheric structure of the Central Andes, I also evaluated the isostatic state of the region. The Nazca plate and western part of the Central Andes are

characterized by positive residual topography (Ca. -0.20 - 0.78 km), indicating that the two regions are isostatically undercompensated. The extra topography on the Nazca ridge may be attributed to density changes in the subducting Nazca plate. The high density of the subducted Nazca plate causes downward force and works in unison with the low density of the Nazca Ridge to raise the ridge to modern day elevation.

The western part of the Central Andes may be partly supported by dynamic processes in the mantle wedge. The small-scale convective cells in the mantle wedge may be providing partial support to the observed topography. The effects of small-scale convective cells on plate coupling have not been investigated in this study. I leave a more detailed evaluation of the effects of small-scale convective cells on plate coupling for future studies.

REFERENCES

- Allmendinger, R.W., and González, G., 2010, Invited review paper: Neogene to Quaternary tectonics of the coastal Cordillera, northern Chile: *Tectonophysics*, v. 495, p. 93–110, doi:10.1016/j.tecto.2009.04.019.
- Allmendinger, R.W., Jordan, T.E., Kay, S.M., and Isacks, B.L., 1997, THE EVOLUTION OF THE ALTIPLANO-PUNA PLATEAU OF THE CENTRAL ANDES: *Annual Review of Earth and Planetary Sciences*, v. 25, p. 139–174, doi:10.1146/annurev.earth.25.1.139.
- Álvarez, O., Nacif, S., Spagnotto, S., Folguera, A., Gimenez, M., Chlieh, M., and Braitenberg, C., 2015, Gradients from GOCE reveal gravity changes before Pisagua Mw = 8.2 and Iquique Mw = 7.7 large megathrust earthquakes: *Journal of South American Earth Sciences*, v. 64, p. 273–287, doi:10.1016/j.jsames.2015.09.014.
- Álvarez, O., Nacif, S., Gimenez, M., Folguera, A., and Braitenberg, C., 2014, GOCE derived vertical gravity gradient delineates great earthquake rupture zones along the Chilean margin: *Tectonophysics*, v. 622, p. 198–215, doi:10.1016/j.tecto.2014.03.011.
- Amante, C., and Eakins, B.W.W., 2009, ETOPO1 – 1 arc-minute global relief model: Procedures, data sources and analysis:, doi:10.1594/PANGAEA.769615.
- Andersen, O.B., Knudsen, P., and Berry, P.A.M., 2010, The DNSC08GRA global marine gravity field from double retracked satellite altimetry: *Journal of Geodesy*, v. 84, p. 191–199, doi:10.1007/s00190-009-0355-9.
- Baranov, B. V., Ivashchenko, A. I., & Dozorova, K. A., 2015, The Great 2006 and 2007 Kuril Earthquakes, Forearc Segmentation and Seismic Activity of the Central Kuril Islands Region. *Pure and Applied Geophysics*, 172(12), 3509–3535.
<https://doi.org/10.1007/s00024-015-1120-z>
- Barckhausen, U., Ranero, C. R., Cande, S. C., Engels, M., & Weinrebe, W., 2008, Birth of an intraoceanic spreading center. *Geology*, 36(10), 767–770.
<https://doi.org/10.1130/G25056A.1>
- Bilek, S.L., 2010, Invited review paper: Seismicity along the South American subduction zone: Review of large earthquakes, tsunamis, and subduction zone complexity: *Tectonophysics*, v. 495, p. 2–14, doi:10.1016/j.tecto.2009.02.037.

- Bürgmann, R., Kogan, M.G., Steblov, G.M., Hilley, G., Levin, V.E., and Apel, E., 2005, Interseismic coupling and asperity distribution along the Kamchatka subduction zone: *Journal of Geophysical Research: Solid Earth*, v. 110, p. 1–17, doi:10.1029/2005JB003648.
- Calderón, M. et al., 2012, The low-grade Canal de las Montañas Shear Zone and its role in the tectonic emplacement of the Sarmiento Ophiolitic Complex and Late Cretaceous Patagonian Andes orogeny, Chile: *Tectonophysics*, doi:10.1016/j.tecto.2011.12.034.
- Charrier, R., Hérail, G., Pinto, L., García, M., Riquelme, R., Farías, M., and Muñoz, N., 2013, Cenozoic tectonic evolution in the Central Andes in northern Chile and west central Bolivia: Implications for paleogeographic, magmatic and mountain building evolution: *International Journal of Earth Sciences*, doi:10.1007/s00531-012-0801-4.
- Chlieh, M., Perfettini, H., Tavera, H., Avouac, J.P., Remy, D., Nocquet, J.M., Rolandone, F., Bondoux, F., Gabalda, G., and Bonvalot, S., 2011, Interseismic coupling and seismic potential along the Central Andes subduction zone: *Journal of Geophysical Research: Solid Earth*, v. 116, doi:10.1029/2010JB008166.
- Chulick, G.S., Detweiler, S., and Mooney, W.D., 2013, Seismic structure of the crust and uppermost mantle of South America and surrounding oceanic basins: *Journal of South American Earth Sciences*, doi:10.1016/j.jsames.2012.06.002.
- Cisternas, M. et al., 2005, Predecessors of the giant 1960 Chile earthquake: *Nature*, v. 437, p. 404–407, doi:10.1038/nature03943.
- Comte, D., and Pardo, M., 1991, Reappraisal of great historical earthquakes in the northern Chile and southern Peru seismic gaps: *Natural Hazards*, doi:10.1007/BF00126557.
- Comte, D., Battaglia, J., Thurber, C., Zhang, H., Dorbath, L., Glass, B., 2004. High-resolution subducting slab structure beneath northern Chile using the double-difference tomography metho. *Eos Trans. AGU* 85 (47). Fall Meet. Suppl., Abstract S53B-0200
- Curtis, M.L., Flowerdew, M.J., Riley, T.R., Whitehouse, M.J., and Daly, J.S., 2010, Andean sinistral transpression and kinematic partitioning in South Georgia: *Journal of Structural Geology*, doi:10.1016/j.jsg.2010.02.002.
- Dorbath, L., Cisternas, A., and Dorbath, C., 1990, Assessment of the size of large and great historical earthquakes in Peru: *Bulletin of the Seismological Society of America*, v. 80, p. 551–576, doi:10.1007/s00217-013-2125-4.
- Echternacht, F., Tauber, S., Eisel, M., Brasse, H., Schwarz, G., and Haak, V., 1997, Electromagnetic study of the active continental margin in northern Chile: *Physics of the Earth and Planetary Interiors*, doi:10.1016/S0031-9201(96)03261-X.

- Folguera, A., and Ramos, V.A., 2011, Repeated eastward shifts of arc magmatism in the Southern Andes: A revision to the long-term pattern of Andean uplift and magmatism: *Journal of South American Earth Sciences*, doi:10.1016/j.jsames.2011.04.003.
- Förste, C. et al., 2014, EIGEN-6C4 - The latest combined global gravity field model including GOCE data up to degree and order 1949 of GFZ Potsdam and GRGS Toulouse: EGU General Assembly, v. 16, p. 3707, doi:http://dx.doi.org/10.5880/icgem.2015.1.
- Gunnell, Y., Thouret, J.-C., Bricchau, S., Carter, A., and Gallagher, K., 2010, Low-temperature thermochronology in the Peruvian Central Andes: implications for long-term continental denudation, timing of plateau uplift, canyon incision and lithosphere dynamics: *Journal of the Geological Society*, doi:10.1144/0016-76492009-166.
- Gutscher, M.A., Spakman, W., Bijwaard, H., and Engdahl, E.R., 2000, Geodynamics of flat subduction: Seismicity and tomographic constraints from the Andean margin: *Tectonics*, v. 19, p. 814–833, doi:10.1029/1999TC001152.
- Husen, S., Kissling, E., and Flueh, E.R., 2000, Local earthquake tomography of shallow subduction in north Chile: A combined onshore and offshore study: *Journal of Geophysical Research*, v. 105, p. 28183, doi:10.1029/2000JB900229.
- Jaramillo, J.S., Cardona, A., León, S., Valencia, V., and Vinasco, C., 2017, Geochemistry and geochronology from Cretaceous magmatic and sedimentary rocks at 6°35' N, western flank of the Central cordillera (Colombian Andes): Magmatic record of arc growth and collision: *Journal of South American Earth Sciences*, doi:10.1016/j.jsames.2017.04.012.
- Krabbenhöft, A., Bialas, J., Kopp, H., Kukowski, N., and Hübscher, C., 2004, Crustal structure of the Peruvian continental margin from wide-angle seismic studies: *Geophysical Journal International*, v. 159, p. 749–764, doi:10.1111/j.1365-246X.2004.02425.x.
- Kumar, A., 2015, Intermediate-depth earthquakes, slab stress state and upper mantle structure beneath the north central Andes [Ph.D. thesis]: Chapel Hill, University of North Carolina, 206 p.
- Lallemand, S., Heuret, A., and Boutelier, D., 2005, On the relationships between slab dip, back-arc stress, upper plate absolute motion, and crustal nature in subduction zones: *Geochemistry, Geophysics, Geosystems*, v. 6, doi:10.1029/2005GC000917.
- Laske, G., Masters, G., Ma, Z., Pasyanos, M.E., and Livermore, L., 2013, Update on CRUST1.0: A 1-degree Global Model of Earth's Crust: *Geophys. Res. Abstracts*, 15,.
- Lay, T., Yue, H., Brodsky, E.E., and An, C., 2014, The 1 April 2014 Iquique, Chile, Mw 8.1 earthquake rupture sequence: *Geophysical Research Letters*, v. 41, p. 3818–3825, doi:10.1002/2014GL060238.

- Lomnitz, C., 2004, Major Earthquakes of Chile: A Historical Survey, 1535-1960: *Seismological Research Letters*, v. 75, p. 368–378, doi:10.1785/gssrl.75.3.368.
- Mahatsente, R., and Ranalli, G., 2004, Time evolution of negative buoyancy of an oceanic slab subducting with varying velocity: *Journal of Geodynamics*, doi:10.1016/j.jog.2004.05.002.
- Meng, L., Huang, H., Bürgmann, R., Ampuero, J.P., and Strader, A., 2015, Dual megathrust slip behaviors of the 2014 Iquique earthquake sequence: *Earth and Planetary Science Letters*, v. 411, p. 177–187, doi:10.1016/j.epsl.2014.11.041.
- Moreno, M.S., Bolte, J., Klotz, J., and Melnick, D., 2009, Impact of megathrust geometry on inversion of coseismic slip from geodetic data: Application to the 1960 Chile earthquake: *Geophysical Research Letters*, v. 36, doi:10.1029/2009GL039276.
- Moreno, M., Rosenau, M., and Oncken, O., 2010, 2010 Maule earthquake slip correlates with pre-seismic locking of Andean subduction zone: *Nature*, doi:10.1038/nature09349.
- Moreno, M. et al., 2011, Heterogeneous plate locking in the South-Central Chile subduction zone: Building up the next great earthquake: *Earth and Planetary Science Letters*, v. 305, p. 413–424, doi:10.1016/j.epsl.2011.03.025.
- Mpodozis, C., and Ramos, V.A., 1989, The Andes of Chile and Argentina: Geology of the Andes and Its Relation to Hydrocarbon and Mineral Resources, doi:10.1016/j.aqpro.2013.07.003.
- Nafe, J.E., Drake, C.L., 1957. Variation with depth in shallow and deep water marine sediments of porosity, density and the velocities of compressional and shear waves. *Geophysics* 22 (3), 523-552
- Norabuena, E.O., Snoke, J.A., and James, D.E., 1994, Structure of the subducting Nazca plate beneath Peru: *Journal of Geophysical Research*, doi:10.1029/94JB00126.
- Oncken, O. et al., 2003, Seismic imaging of a convergent continental margin and plateau in the central Andes (Andean Continental Research Project 1996 (ANCORP'96): *Journal of Geophysical Research: Solid Earth*, doi:10.1029/2002JB001771.
- Pardo-Casas, F., and Molnar, P., 1987, Relative motion of the Nazca (Farallon) and South American Plates since Late Cretaceous time: *Tectonics*, doi:10.1029/TC006i003p00233.
- Pasyanos, M.E., Masters, T.G., Laske, G., and Ma, Z., 2014, LITHO1.0: An updated crust and lithospheric model of the Earth: *Journal of Geophysical Research: Solid Earth*, doi:10.1002/2013JB010626.
- Pavlis, N.K., Holmes, S.A., Kenyon, S.C., and Factor, J.K., 2013, Erratum: Correction to the development and evaluation of the earth gravitational model 2008 (EGM2008): *Journal of Geophysical Research: Solid Earth*, v. 118, p. 2633, doi:10.1002/jgrb.50167,2013.

- Prezzi, C.B., Götze, H.J., and Schmidt, S., 2009, 3D density model of the Central Andes: Physics of the Earth and Planetary Interiors, doi:10.1016/j.pepi.2009.09.004.
- Proshkina, Z. N., Kulinich, R. G., & Valitov, M. G. ,2017, Structure, Matter Composition, and Deep Structure of the Oceanic Slope of the Central Kuril Islands: New Evidence. *Russian Journal of Pacific Geology*, 11(6), 436–446. <https://doi.org/10.1134/s1819714017060045>
- Ramos, V.A., 2010, The Grenville-age basement of the Andes: Journal of South American Earth Sciences, doi:10.1016/j.jsames.2009.09.004.
- Ray, J.S., Mahoney, J.J., Duncan, R.A., Ray, J., Wessel, P., and Naar, D.F., 2012, Chronology and geochemistry of lavas from the Nazca Ridge and Easter Seamount Chain: An ~30 myr hotspot record: Journal of Petrology, v. 53, p. 1417–1448, doi:10.1093/petrology/egs021.
- Ruiz, S., Metois, M., Fuenzalida, A., Ruiz, J., Leyton, F., Grandin, R., Vigny, C., Madariaga, R., and Campos, J., 2014, Intense foreshocks and a slow slip event preceded the 2014 Iquique Mw8.1 earthquake: Science, doi:10.1126/science.1256074.
- Rutland, R.W.R., 1971, Andean orogeny and ocean floor spreading: Nature, doi:10.1038/233252a0.
- Rutledge, S., and Mahatsente, R., 2017, Fore-arc structure, plate coupling and isostasy in the Central Andes: Insight from gravity data modelling: Journal of Geodynamics, v. 104, p. 27–35, doi:10.1016/j.jog.2016.12.003.
- Satake, K., Shimazaki, K., Tsuji, Y., and Ueda, K., 1996, Time and size of a giant earthquake in Cascadia inferred from Japanese tsunami records of January 1700: Nature, v. 379, p. 246–249, doi:10.1038/379246a0.
- Schaller, T., Andersen, J., Götze, H.J., Koproch, N., Schmidt, S., Sobiesiak, M., and Splettstößer, S., 2015, Segmentation of the Andean margin by isostatic models and gradients: Journal of South American Earth Sciences, v. 59, p. 69–85, doi:10.1016/j.jsames.2015.01.008.
- Scheuber, E., and Reutter, K.J., 1992, Magmatic arc tectonics in the Central Andes between 21° and 25°S: Tectonophysics, doi:10.1016/0040-1951(92)90422-3.
- Scheuber, E., Bogdanic, T., Jensen, A., and Reutter, K.-J., 2012, Tectonic Development of the North Chilean Andes in Relation to Plate Convergence and Magmatism Since the Jurassic, *in* Tectonics of the Southern Central Andes, doi:10.1007/978-3-642-77353-2_9.
- Schilling, F.R., Partzsch, G.M., Brasse, H., and Schwarz, G., 1997, Partial melting below the magmatic arc in the central Andes deduced from geoelectromagnetic field experiments and laboratory data: Physics of the Earth and Planetary Interiors, doi:10.1016/S0031-9201(97)00011-3.

- Schurr, B. et al., 2014, Gradual unlocking of plate boundary controlled initiation of the 2014 Iquique earthquake: *Nature*, doi:10.1038/nature13681.
- Sobolev, S. V., and Babeyko, A.Y., 1994, Modeling of mineralogical composition, density and elastic wave velocities in anhydrous magmatic rocks: *Surveys in Geophysics*, doi:10.1007/BF00690173.
- Somoza, R., 1998, Updated Nazca (Farallon)-South America relative motions during the last 40 My: Implications for mountain building in the central Andean region: *Journal of South American Earth Sciences*, doi:10.1016/S0895-9811(98)00012-1.
- Somoza, R., and Zaffarana, C.B., 2008, Mid-Cretaceous polar standstill of South America, motion of the Atlantic hotspots and the birth of the Andean cordillera: *Earth and Planetary Science Letters*, doi:10.1016/j.epsl.2008.04.004.
- Steinberger, B., Conrad, C.P., Osei Tutu, A., and Hoggard, M.J., 2017, On the amplitude of dynamic topography at spherical harmonic degree two: *Tectonophysics*, doi:10.1016/j.tecto.2017.11.032.
- Tassara, A., 2005, Interaction between the Nazca and South American plates and formation of the Altiplano-Puna plateau: Review of a flexural analysis along the Andean margin (15°-34°S): *Tectonophysics*, v. 399, p. 39–57, doi:10.1016/j.tecto.2004.12.014.
- Tassara, A., Götze, H.J., Schmidt, S., and Hackney, R., 2006, Three-dimensional density model of the Nazca plate and the Andean continental margin: *Journal of Geophysical Research: Solid Earth*, doi:10.1029/2005JB003976.
- Tassara, A., 2010, Control of forearc density structure on megathrust shear strength along the Chilean subduction zone: *Tectonophysics*, v. 495, p. 34–47, doi:10.1016/j.tecto.2010.06.004.
- Utsu, T., 1999, Representation and Analysis of the Earthquake Size Distribution: A Historical Review and Some New Approaches: *pure and applied geophysics*, v. 155, p. 509–535, doi:10.1007/s000240050276.
- Van Hunen, J., Van Den Berg, A.P., and Vlaar, N.J., 2002, On the role of subducting oceanic plateaus in the development of shallow flat subduction: *Tectonophysics*, doi:10.1016/S0040-1951(02)00263-9.
- van Hunen, J., van den Berg, A.P., and Vlaar, N.J., 2002, The impact of the South-American plate motion and the Nazca Ridge subduction on the flat subduction below South Peru: *Geophysical Research Letters*, doi:10.1029/2001gl014004.
- von Huene, R., and Ranero, C.R., 2003, Subduction erosion and basal friction along the sediment-starved convergent margin off Antofagasta, Chile: *Journal of Geophysical Research: Solid Earth*, doi:10.1029/2001jb001569.

- von Huene, R., and Scholl, D.W., 1991, Observations at convergent margins concerning sediment subduction, subduction erosion, and the growth of continental crust: *Reviews of Geophysics*, doi:10.1029/91RG00969.
- Wang, K., and Bilek, S.L., 2011, Do subducting seamounts generate or stop large earthquakes? *Geology*, doi:10.1130/G31856.1.
- Wigger, P.J. et al., 2012, Variation in the Crustal Structure of the Southern Central Andes Deduced from Seismic Refraction Investigations, *in* *Tectonics of the Southern Central Andes*, doi:10.1007/978-3-642-77353-2_2.
- Wirth, E.A., and Korenaga, J., 2012, Small-scale convection in the subduction zone mantle wedge: *Earth and Planetary Science Letters*, doi:10.1016/j.epsl.2012.09.010.
- Woods, M.T., and Okal, E.A., 1994, The Structure of the Nazca Ridge and Sala Y Gomez Seamount Chain From the Dispersion of Rayleigh Waves: *Geophysical Journal International*, doi:10.1111/j.1365-246X.1994.tb03313.x.
- Yagi, Y., Okuwaki, R., Enescu, B., Hirano, S., Yamagami, Y., Endo, S., and Komoro, T., 2014, Rupture process of the 2014 Iquique Chile earthquake in relation with the foreshock activity: *Geophysical Research Letters*, v. 41, p. 4201–4206, doi:10.1002/2014GL060274.
- Yuan, X. et al., 2000, Subduction and collision processes in the Central Andes constrained by converted seismic phases: *Nature*, v. 408, p. 958–961, doi:10.1038/35050073.

APPENDIX

Codes written for gravity corrections and analysis. :

```
% %Data Filtering with the use of FFT
% close all
% clear all
% clc
% %Data Upload
% data=load('Lab_9_Input');
% data_Lat=data(:,1);% Lat
% data_Long=data(:,2);% Long
% data_BA=data(:,3);% Bouger anomaly
%
% % Reshaping of the data for 2D plot
%
% Rdata_Lat=reshape(data_Lat,251,251);
% Rdata_Long=reshape(data_Long,251,251);
% Rdata_BA=reshape(data_BA,251,251);

%Fourier Transformation
F_BA = fft2(Terrcalc);
asdf = ifft2(F_BA);
% size(Rdata_BA)
% size(F_BA)
%intervals in wave number domain

dx=1.11 ;%interval in physical space(km)
dkx=(2.0*pi)/(size(Terrcalc,1)*dx);%Spacing of the grid points: 2pi/N(using the size of the
second dimension of Rdata_BA), where N is the size of the data
kx=[0: round(size(F_BA,1)/2 -1) round(-size(F_BA,1)/2 +1) :-1]*dkx; % wavenumber
coordinates in the kx direction
%Elements of K are(0,1,...N/2,-N/2 +1, -N/2 +2. -1)
dky=(2.0*pi)/(size(Terrcalc,2)*dx); %spacing of the grid points: 2pi/N (using the size of the
second dimension of Rdata_BA)
ky=[0: round(size(F_BA,2)/2 -1) round(-size(F_BA,2)/2 +1) :-1]*dky; % wavenumber
coordinates in the ky direction
%Elements of K are(0,1,...N/2,-N/2 +1, -N/2 +2. -1)
% size(kx)
```

```

% size(ky)
%computational components of wavenumber
for i=1:length(kx);
    for j=1:length(ky);
kr(i,j)=sqrt(kx(i).^2 + ky(j).^2);%Radial wavenumber

%Regional- Residual Separation
con_1=(2*pi)/290;%Threshold wavelength = 50km

if kr(i,j) > con_1;%supressing the short wavelength
    F_Reg_Lfilt (i,j)=F_BA(i,j)*0.0; %If the radial wavenumber is greater than 50km, suppress
else F_Reg_Lfilt (i,j)=F_BA(i,j)*1.0;%Radial wavenumbers less than 50km will be kept
end
%
% if kr(i,j) < con_1;%supressing the long wavelength
%   F_Reg_Sfilt (i,j) = F_BA(i,j)*0.0; %If radial is less than 50km, suppress
% else
%   F_Reg_Sfilt (i,j) = F_BA(i,j)*1.0; %Radial greater than 50km will be kept
% end
end
end

F_RES_INV_L = ifft2(F_Reg_Lfilt); %inverse Fourier transformation of raidal wavenumbers
that are kept by the filter to get back to the space domain
% F_RES_INV_S = ifft2(F_Reg_Sfilt); %dilly dilly (above)

% %Continuation filter
% Z=10;
% G_Up = F_BA.*exp(-kr*Z); %Upward Continuation @ Z
% G_Up_Inv = ifft2(G_Up);
%
% D=0.5
% G_Down = F_BA.*exp(kr*D);
% G_Down_Inv = ifft2(G_Down);

figure(1)
[c,h]=contourf(Rdata_Long,Rdata_Lat,Terrcalc);
%shading interp
h=colorbar;
% axis([-3000 3000 -3000 3000])
title('Bouger anomaly (Original Data)', 'fontweight','bold')
xlabel('Long')
ylabel('Lat')
title (h,['mGal'])

```

```

figure(2)
[c,h]=contourf(Rdata_Long,Rdata_Lat,F_RES_INV_L);
%shading interp
h=colorbar;
title('Bouger anomaly (Long Wavelength Filtered Data)', 'fontweight','bold')
xlabel('Long')
ylabel('Lat')
title(h,['mGal'])

```

```

figure(5)
[c,h]=contourf(Rdata_Long,Rdata_Lat,G_Up_Inv);
%shading interp
h=colorbar;
title('Upward Continuation at 1km')
xlabel('Longitude')
ylabel('Latitude')
%

```

```

% figure(6)
% [c,h]=contourf(Rdata_Long,Rdata_Lat,G_Down_Inv);
% %shading interp
% h=colorbar;
% title('Downward Continuation at 0.5km')
% xlabel('Longitude')
% ylabel('Latitude')

```

Dynamic Topography:

```

clc
clear all
close all

```

```

% rho_a = 3230; %kg/m^2 density of astenosphere
% rho_c = 2800; %kg/m^2 density of crust
% rho_l = 3200; %kg/m^2 density of lithosphere
% h = -2.6;%average ridge elevation in km

```

```

rho_m = 3200;
rho_a = 3350; %kg/m^2 density of astenosphere
%rho_c = 2800; %kg/m^2 density of crust
rho_l = 3200; %kg/m^2 density of lithosphere
h = 2.6;%average ridge elevation in km
rho_CC_crust=2800;
rho_OC_crust=2980;
rho_water=1027;

```

```

%uploading data
topo1 = xlsread('Topo-1.xlsx');

```

```

Long = xlsread('Long-1.xlsx');
Lat = xlsread('lat-1.xlsx');
Crust = xlsread('CrustModel.xlsx');
LAB = xlsread('LAB.xlsx');
a=reshape(Crust, [11,13]);
C_avg = 32; %average global crust thickness in km

% figure(14)
% [c,h]=contourf(Long,Lat,a);
% h=colorbar;
% figure(15)
% [c,h]=contourf(Long,Lat,LAB);
% h=colorbar;

% %Expected Topo
% for i=1:11;
%   for j=1:13;
%     e_t(i,j) = (((rho_a - rho_c)/(rho_a))*(a(i,j) - C_avg) + ((rho_a - rho_l)/(rho_a))*(LAB(i,j)
- C_avg)) - 2.6;
%     d_t(i,j) = (topo1(i,j) - e_t(i,j));
%   end
% end

%Expected Topo
for i=1:11;
  for j=1:13;

    if topo1(i,j) >=0;
      rho_c = rho_CC_crust;

e_t(i,j) = (((a(i,j)-32.0)*(rho_m - rho_c))/(rho_m)) + (((LAB(i,j)-50)*(rho_a - rho_l))/rho_a);
      % d_t(i,j) = (e_t(i,j) - topo1(i,j));
      d_t(i,j) = topo1(i,j)- (e_t(i,j));
      else
      rho_c = rho_OC_crust;

e_t(i,j) = (((a(i,j)-32)*(rho_m - rho_c))/(rho_m - rho_water)) + (((LAB(i,j)- 50)* (rho_a -
rho_l))/rho_a);
      % d_t(i,j) = (e_t(i,j) - topo1(i,j));
      d_t(i,j) = topo1(i,j)-( e_t(i,j));
      end

    end
  end
end

```

```
% figure(2)
% [c,h]=contourf(Long,Lat,LAB);
% h=colorbar;
figure(10)
[c,h]=contourf(Long,Lat,d_t,50);
set(h,'LineColor','none');
colormap('default');
h=colorbar;
colormap(jet)
figure(8)
[c,h]=contourf(Long,Lat,e_t,50);
set(h,'LineColor','none');
colormap('default');
h=colorbar;
figure(9)
[c,h]=contourf(Long,Lat,topo1,50);
set(h,'LineColor','none');
colormap('default');
h=colorbar;
```